Universidade Federal do Rio Grande do Sul

Arthur Casa Nova Nonnig

Magnetotransport in Bismuth/Cobalt Multilayers: Rationalizing Spin-Orbit Proximity Effect

Porto Alegre, RS, Brazil

2021

Arthur Casa Nova Nonnig

Magnetotransport in Bismuth/Cobalt Multilayers: Rationalizing Spin-Orbit Proximity Effect

Dissertação realizada sob a orientação do Prof. Dr. Milton Andre Tumelero e apresentada para o Programa de Pós-Graduação em Física da Universidade Federal do Rio Grande do Sul, em cumprimento parcial dos requisitos para a obtenção do título de Mestre em Física.

Universidade Federal do Rio Grande do Sul - UFRGS

Instituto de Física

Supervisor: Milton Andre Tumelero

Co-supervisor: Paulo Pureur Neto

Porto Alegre, RS, Brasil

2021

Agradecimentos

Ao meu estimado orientador, Professor Milton Andre Tumelero, por toda atenção, conhecimento e dedicação durante todo meu período como aluno de IC voluntária e mestrado.

Aos professores do Laboratório, Prof. Paulo Pureur, meu coorientador, e Fabiano Mesquita, pelos ensinamentos na física experimental.

À minha amada Jéssica, por todo carinho e apoio durante o período de mestrado.

À minha família, por me dar a oportunidade de seguir uma nova carreira após uma primeira graduação.

Aos amigos que conheci no IF, aos colegas do Laboratório, pelas conversas nos corredores e momentos de descontração.

Ao CNPq, pelo fornecimento da minha bolsa de mestrado com número de processo 144443/2019-8 que permitiu realizar esta pesquisa.

A cada pesquisador brasileiro que resiste lutando pela Ciência e Educação em um cenário de desvalorização da produção científica.

Resumo para público leigo

Neste trabalho, utilizou-se o cobalto, metal de transição com número atômico 27, amplamente estudado desde o período da chamada física clássica por ter características ferromagnéticas. Também trabalhou-se com o bismuto, metal diamagnético de 83 prótons em seu "grande" átomo, com poder de interação spin-órbita, foco deste trabalho. A interação assim chamada é uma interação oriunda do movimento orbital das cargas e do spin, característica intrínseca dos elétrons. Para analisar a interação entre esses metais, criaram-se estruturas de multicamadas, como sanduíches, em que cada nova camada (filme fino) é composta por um metal, intercalando sempre Cobalto e Bismuto, alterando a espessura de cada metal em determinada amostra. A espessura desse "sanduíche metálico" é ínfima se comparada com objetos do dia a dia, cerca de centenas de milhares de vezes menor. Cada camada utilizada nessas amostras tem 0,000000001 metro, ou seja, para entender como é a interação, buscou-se desenvolver uma estrutura de dimensões pequenas, pois assim as características de cada metal separado se tornam menos preponderantes, enquanto a região de interação ganha maior proeminência. Para analisar tal relação entre os metais, as amostras foram expostas a variáveis campos magnéticos, diferentes temperaturas e correntes elétricas para que, desta forma, fosse possível caracterizar e analisar a interação a partir de fenômenos já conhecidos, sob uma perspectiva da interação spin-órbita. Dito isso, durante os experimentos, observou-se mudanças na resistência elétrica da amostra, que não pode ser simplesmente entendida como a soma dos dois componentes. Além disso, em temperaturas muito baixas (abaixo de -240°C), a resistência teve um aumento inesperado. A resistência elétrica das amostras em presença de campo magnético também mostrou comportamentos inusitados, apresentando um pico em amostras com determinada espessura de Cobalto. O comportamento magnético esperado pelo Cobalto também teve alteração pela presença do Bismuto. Todas essas observações, são embasadas por trabalhos anteriores, no entanto, esse estudo contribui com informações originais para o contexto de interação entre metais ferromagnéticos mediada pelo acoplamento spin-órbita.

Abstract

The interplay between strong spin-orbit coupling (SOC) and magnetization at interfaces has been a pathway for the observation of novel physical phenomena, quasi-particles and potential for design new devices. The interfaces formed by ferromagnetic materials (FM) materials and with strong SOC are strongly improved by proximity effects which allow the introduction of unexpected electronic properties in the system. It is possible to list many examples like the presence of Skyrmions on the surface of FM transition metal/heavy metals multilayers and the observation of spin-orbit torque in topological insulator and ferromagnetic metal interface. In this work, we use multilayers of Bismuth and Cobalt, as SOC and FM materials, respectively, in order to look for anomalies in magnetization and electrical transport induced at the interfaces. Even though the bismuth is not a topological insulator, it presents a strong SOC. The samples were produced by using magnetron sputtering. Multilayers of Bi(x)/Co(y) with x and y in between 0.5 and 3nm, containing about 10x repetition were grown on top of SiO2/Si wafer. The samples were characterized with magnetization and electrical transport in between 3 K and 300 K. From electrical transport experiments we observed an unexpected increase of the resistance. Both Anomalous Hall Effect and Anomalous Magnetoresistance indicate the occurrence of an enhancement of SOC at the Co layers induced by the Bi layer.

Keywords: spin-orbit coupling; magnetotrasport; magnetoresistance; thin films;

Resumo

A interação entre o acoplamento spin-órbita (SOC) e magnetização em interfaces tem sido um caminho para a observação de novos fenômenos físicos, quase-partículas e potencial para projetar novos dispositivos. As interfaces formadas por materiais ferromagnéticos (FM) e com forte SOC são fortemente potencializadas por efeitos de proximidade, que permitem a introdução de propriedades eletrônicas inesperadas ao sistema. É possível listar muitos exemplos, como a presença de Skyrmions na superfície de multicamadas de metal de transição FM e metais pesados e a observação de torque spin-órbita em isolante topológico e interface de metal ferromagnético. Neste trabalho de mestrado, usamos multicamadas de bismuto e cobalto, como materiais SOC e FM, respectivamente, a fim de procurar anomalias na magnetização e transporte elétrico induzido nas interfaces. Embora o bismuto não seja um isolante topológico, ele apresenta um forte SOC. As amostras foram produzidas usando magnetron sputtering. Multicamadas de Bi (x) / Co (y) com xey entre 0,5 e 3nm, contendo cerca de 10x de repetição, foram cultivadas no topo da pastilha de SiO2 / Si. As amostras foram caracterizadas com magnetização e transporte elétrico entre 3 K e 300 K. Resultados do magnetotransporte do efeito Hall anômalo e de magnetorresistência anômala apontam para um aumento do SOC nas camadas de Co induzido pela camada Bi.

Palavras-chave: acoplamento spin-órbita; magneto-transporte; magnetorresistência; filmes finos;

List of Figures

List of Tables

List of abbreviations and acronyms

SOC	Spin-orbit coupling
FM	Ferromagnetic Material
Co	Cobalt
Bi	Bismuth
CFA	CoFeAl alloy
MR	Magnetoresistance
M	Magnetization
H	Applied Magnetic Field
RF	Radio-Frequency
AMR	Anisotropic Magnetoresistance
OMR	Ordinary Magnetoresistance
LMR	Longitudinal Magnetoresistance
TMR	Transversal Magnetoresistance
PMR	Perpendicular Magnetoresistance
AHE	Anomalous Hall Effect
AHR	Anomalous Hall Resistivity
RBS	Rutherford Backscattering Spectrometry
XRD	X-ray Diffraction
GIXRD	Grazing Incidence X-ray Diffraction
DFT	Density Functional Theory
VSM	Vibrating Sample Magnetometer

DMI	Dzyaloshinskii–Moriya interaction
DOS	Density of States
DC	Direct Current
SOPE	Spin-Orbit Proximity Effect
SOE	Spin-Orbit Energy

List of symbols

H_{DM}	Dzyaloshinskii–Moriya field
T	Temperature
T_C	Critical Temperature
M	Magnetization
H	Magnetic Field
Ms	Spontaneous Magnetization
e	Elementary electric charge
t	Time
p	Momentum
m_e	Electron mass
$\hbar$	Reduced Planck's constant
μ	Magnetic Moment
μ_B	Bohr Magneton
Z	Atomic Number
v	Velocity
μ_0	Vacuum permeability
B	Magnetic Induction field vector
B	Effective Magnetic Induction field vector
E	Electric Field vector
ΔH	Variation of energy
αH	Spin-orbit coupling constant

c	Speed of light in vacuum
$\sigma_{x,y,z}$	Pauli matrices
k	Wave number
σ	Rashba coupling parameter
ρ	Resistivity
θ	Angle
J	Current density
R_0	Ordinary Hall Effect Coefficient
R_s	Anomalous Hall Effect Coefficient
λ	X-ray wavelength

Contents

Introduction

The search for new emergent electronics phases in matter with potential to highlight new physics phenomena and enhance technological applications have being a major challenge in condensed matter physics, mostly in solid state physics. In recent years, it has been shown that the interplay between strong spin-orbit coupling (SOC) and ferromagnetic ordering (FM) is a very good way to pave such road to science development. Among some interesting physics rising in systems with high-SOC and FM we can cite the skyrmions [13] and the Anomalous Quantum Hall Insulators [14, 15] (which are topological insulators with ferromagnetic properties). The whole picture becomes much more exciting at the interfaces, where the translation symmetry breaks and the proximity effects are new ingredients to induce novel physical phenomena and probably is the most promising pathway to advance our knowledge in solid state physics and designing new spintronic and quantum devices. Figure 0.1 shows a schematic of several phases, phenomena and application that can originate from interaction of spin-orbit and magnetism.

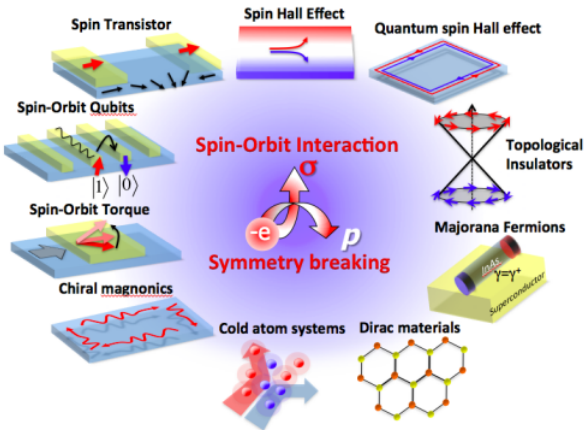

Figure 0.1 – Application of SOC in different areas of Physics. Adapted from [1]

At interfaces formed by materials with strong SOC and a ferromagnetic, the hybridization of p-orbitals, the broken inversion symmetry, and the proximity effects that could arise make the physical description complex and give rise to a rich and exotic phenomena [16]. In this work we will focus on the proximity effects, mainly in the case of spin-orbit coupling, which will allow the observation of unexpected electronic properties to the system. Before we proceed to the results obtained in this work, first some important background should be reviewed, as will be done below.

Let us begin with the exotic magnetic interactions at the interfaces of magnetic het-

erostructures (stacks of FM layers and strong-SOC layers), where the the spin-orbit coupling plays a fundamental role in properties such as: the perpendicular magnetic anisotropy ([17]), and in the creation of skyrmions (magnetic textures with quasi-particle characteristics)([18], [13]). The key interaction to obtain such spin textures is the Dzyaloshinskii–Moriya interaction (DMI) ([19],[20]). This interaction is described by the equation $H_{DM} = D_{ij}s_i \times s_j$. and is characterized by two non-collinear spin sites interacting via a strong spin-orbit site. Two other important consequences of the DMI are the induction of a canting on the spin sites which should be non-parallel and the presence of chirality, once the DMI is an anti-symmetrical interaction. The DMI is responsible to force the spins out-of-plane in ultrathin films [21, 22, 23] and stabilize the skyrmions at FM thin films surfaces [24, 13, 18]. The DMI interaction could occur either in interfaces as well as in bulk materials [25, 26, 13] However, in well designed interfaces at magnetic heteroestructures the DMI could be enhanced by several orders of magnitude [18] Other effects which are closely related to DMI in FM systems are chiral domain walls [27, 28] and domain dumping [29, 30, 31].

The usual layers stacking in magnetic heterostructucture used to enhance the DMI are: Pt/Co/Ta [24], Pd/Co [32], Ru/Co [32], etc. Metallic layers such as Platinum, Palladium, Ruthenium, Iridium, Tantalum, etc. have been used since they are heavy metal and introduce spin-orbit coupling. On the other hand, Cobalt, Iron-Cobalt and Iron have being used as Ferromagnetic layers, mainly due to the high crystalline anisotropy compared to other FM such as Ni and Mn. The asymmetry of the trilayers or the use of a bilayer is a requirement in order to sum up the DMI interaction rising at distinct interfaces [33], necessary to stabilize skyrmions, for instance. Symmetric staking of SOC/FM layers, such as Pt/Co, Pd/Co, have been used to obtain perpendicular anisotropy [34, 35]. SOC layers with thicknesses up to 4 nm have been used, while the FM thicknesses are not thicker than 2 nm.

Another particular utilization of high SOC heterostructures is in ferromagnetic Josephson junctions whose objective is to create a long range triplet supercurrent along ferromagnetic layers by means of the superconductor proximity effect [36]. Notice that usual BCS supercondutores presents only singlet (with no magnetic moment) supercurrent components. In the case of Triplet current, magnetic moment could be carried along with the charge. Thin films of Co, Ru, Nb are the default layers for these types of studies, where Cobalt is the ferromagnetic material, Ruthenium the strong spin-orbit material and Niobium the superconductor [37]. The pair SOC/FM have the function of introduce non-colinear magnetization configuration over

the heterostructure. The non-colinear magnetization act as a filter, changing the interference condition and allowing the spin-triplet component to the supercurrent. Such type of studies aim to enable the, so called, superconducting spintronics, combining heavy metal layers to FM and SC, in order to obtain the ultimate performance in term of magnetoristance. More recently, Amundsen and Linder [38] derived a series of boundary conditions to take a very strong spin-orbit coupling at the interfaces of superconductor-ferromagnet bilayer and in superconductor-ferromagnet-superconductor Josephson junction, demonstrating theoretically the emergence of long-range triplet supercurrent without the necessity of of non-colinear magnetization.

Very interesting properties could be found by taking in account other types of proximity effect. For example, the group of Prof. R. Moodera [39] has shown that in the interface of Bi_2Se_3 topological insulator compound (presenting very high SOC) with the ferromagnetic layer EuS, unconventional magnetic properties could be induced 2 nm below into the Bi_2Se_3, which is related to the so-called ferromagnetic proximity effect. Such phenomena is powered by the strong spin-orbit and leading the spins at the interface align out-of-plane. The robustness of the FM ordering is even stronger than the FM in EuS, showing Curie temperature up to room temperature, while the EuS shows T_c of about 20 K. More recently, Avsar, et al, [40] showed that the spin-orbit coupling can also be extended to other media close to interfaces as a proximity effect. They demonstrated that SOC can be enhanced in graphene by proximity with WS_2, which has strong SOC. Many other demonstrations of SOC proximity effect in graphene layers and other semiconductores systems have being discovered in these last years [41, 42], including in interfaces with Platinum [43, 44]. Notice that the SOC proximity effect in Graphene can drive a topological phase transition turning the Graphene into a topological insulator by the introduction of a band gap at the Dirac point, which has been observed recently [45].

Although the FM and SOC proximity effects seems really efficient to generate new exotic phenomena at interfaces of between FM and SOC materials, its has been only observed in very specific systems. The verification SOC proximity effect in Ferromagnetic materials, or in Ferromagnetic layers still challenging and only few reports on this subject may be found in literature. One interesting work using multilayers of Platinum and a Cobalt-Iron-Aluminium magnetic alloy (CFA) multilayers was published by Zhang, et al, ([2]) in a study of the spin orbit coupling in nonmagnetic metal/ferromagnet bilayers by measuring the anomalous Hall effect. The anomalous Hall coefficient determined by these authors is presented in the Figure 0.2. The data indicates a significant enhancement of the anomalous Hall resistivity (AHR) in the presence

of a layers with strong SOC. The mechanism underlying these enhancement in the AHR is not discussed and the results were presented as a possible evidence of proximity SOC effect. Since the coexistence of strong SOC and FM ordering at interfaces due to proximity effect has a strong potential to produce new discoveries in physics, such as new orderings, new phases and new applications, it is really import to advance in its knowledge.

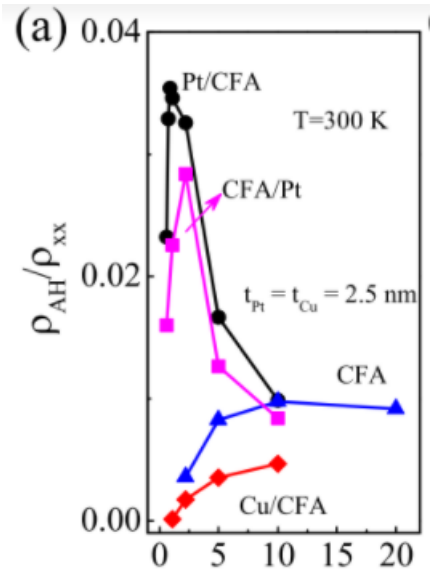

Figure 0.2 – Thickness (nm) dependence of the ratio between the Hall and longitudinal resistivities for Pt/CFA, CFA/Pt, CFA, and Cu/CFA bilayers. Figure adapted from ref. [2]

Another very important element which has very strong SOC is the Bismuth. A simple comparison to Platinum highlights some points such as: The SOC in Bi comes from p-orbital, Bi has much larger electrical resistivity and Bi is more accessible than Platinum. Honda, et al, [3]) explored the alloying of Bismuth and cobalt using the experimental analysis of magnetoresistance (MR) and the Kohler law. They observed a linear rise in saturation-magnetization, while coercivity and resistivity decrease with the increase of Cobalt fraction in comparison to Bismuth content. The transport analysis points to a dependence of the Ordinary magnetoresistance (OMR) and the Anisotropic Magnetoresistance (AMR) on the Bismuth content. The Figure 0.3 shows that magnetoresistance measurements in the BiCo alloys and the MR percentual MR, which indicates that there is a maximum value of AMR for about 15 percent of Cobalt.

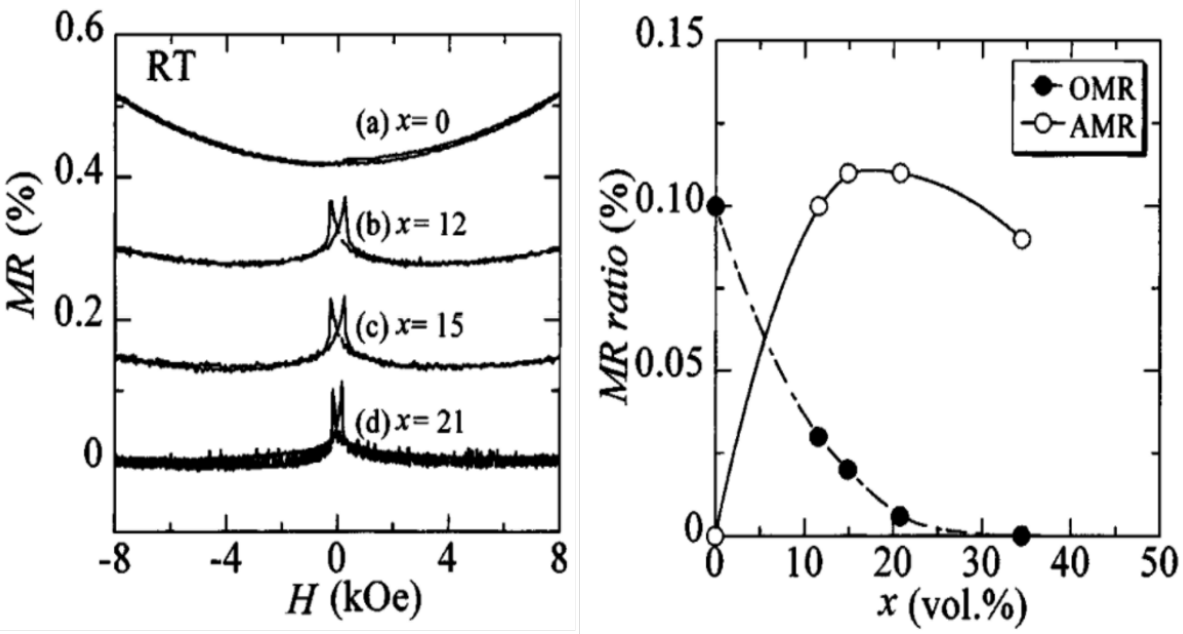

Figure 0.3 – Magnetoresistance of $Bi_{100-x}Co_x$ alloy. (a) MRxH curves for different temperatures and (b) the magnetoresistance ratios for the same alloys. Figure adapted from ref. [3]

In order to advance in the knowledge of synergy between the magnetic properties and the spin-orbit coupling at interfaces, aiming the generation of fundamental understanding to the solid physics as well as for allowing development of future spintronic devices, the present work has the main objective to study the magnetic and transport properties of Bismuth/Cobalt multilayers. Analysing the magnetoresistance and anomalous Hall effect in such samples, our goal is to seek for a better understanding of the proximity effects between a ferromagnetic material and a highly spin-orbit coupling material.

First, we review the essential background for understanding the results that will be presented here, such as ferromagnetism, spin-orbit interaction, properties as the magnetoresistance and the Hall effect. Then we describe the experimental methods, including the sample preparations and characterization. Next, we present the measurements and analyses then prodpose the interpretation of the obtained data. By the end, we conclude and propose further projects to accomplish.

1 Theoretical Basis

In this chapter we will introduce the theoretical basis underlying this thesis and that will be needed to analyse the data that will be presented. In this work, we focused on the investigation of transport and magnetic properties of multilayers intercalating a magnetic material and a high spin-orbit materials. Our focus in this chapter is to proportionate the minimal knowledge for those who are not familiar with the terms and concepts applied in this dissertation. First we will present some notions about the magnetic properties of matter, then we follow with a discussion on the spin-orbit coupling and magnetotransport properties.

1.1 Ferromagnetism

The Ferromagnetism is a fundamental state of matter characterized mainly by two properties. First a spontaneous magnetization occurs at zero external magnetic field. Second, an irreversible nonlinear response of the magnetization (M) to an external field (H), gives rise to a characteristic hysterisis, as shown in Figure 1.1. This phenomena was first studied by James Ewing by the end of the nineteenth century [46].

The spontaneous magnetization in ferromagnets is a consequence of a long range of magnetic moments which are aligned into a parallel configuration. The interaction behind the moment alignment is named the exchange interaction. In a macroscopic sample, large

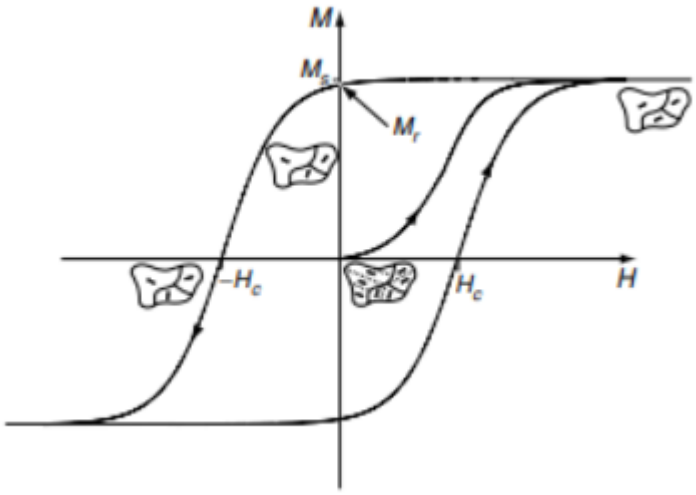

Figure 1.1 – Hysteresis curve for ferromagnetic system. Adapted from [4].

magnetic domains are stabilized. Within each domain, atomic moments are ordered in a parallel configuration. Such domains could have dozens or ever hundreds of nanometers. Different domains are separated by domain walls which are formed to minimize the magnetostatic energy [4, 47].

The hysterisis loop begins in an unmagnetized state, where the magnetic domains are misaligned, with total moment pointing in random directions, given a zero global magnetization in the whole sample. By applying an external magnetic field the domains align to each other leading to an ordered state with a spontaneous magnetization (M_S). The complete ordering is obtained at the maximum magnetization of the sample, known as the saturation magnetization. Another important point of the hysteresis curve is the remnant magnetization (M_R), the magnetization value at which the applied field is null. Is also important to highlight the coercive field, that corresponds to the field at which the magnetization becomes zero after saturation. This field (H_C in Figure 1.1) is opposite to the saturation magnetization. Hard magnetic materials present a square shape hysteresis due to big coercive field and soft magnetic materials are characterized by a narrow hysteresis curve. Soft materials are easily demagnetized and hard material are more difficult to demagnetized [4, 47].

1.2 Spin-orbit Interaction

The spin-orbit coupling (SOC) is a relativistic effect acting on an electron which occurs large orbital velocity and submitted to a high electric field generated by the positive nucleus which together creates a magnetic field strong enough to interact with the spin of the electron [48, 49]. In atomic systems, the spin-orbit coupling can be calculated by assuming that the nucleus orbits around the electron. By using a simple semiclassical toy model, as shown in Figure 1.2, for a Hydrogen atom (with l > 0), in which the magnetic field, generated by the orbital motion of the nucleus, interacts with the spin of the electron, it is possible to estimate the change in energy due to this coupling. To do that, firstly one can estimate the magnetic moment due to the orbital motion,as indicated in Equation 1.1 [5]

$$\mu_{\mathbf{l}} = -\frac{e}{2m_e}\mathbf{l} = -(\frac{\mu_B}{\hbar}) \cdot \mathbf{l} \tag{1.1}$$

Then the magnetic field due to this magnetic moment, is given by Equation 1.2 [5].

$$\mathbf{B_l} = \frac{\mu_0 Ze}{4\pi r^3}(\mathbf{v} \times -\mathbf{r}) = -\frac{\mu_0 Ze}{4\pi r^3}(\mathbf{v} \times \mathbf{r}) = +\frac{\mu_0 Ze}{4\pi r^3 m_e}\mathbf{l} \tag{1.2}$$

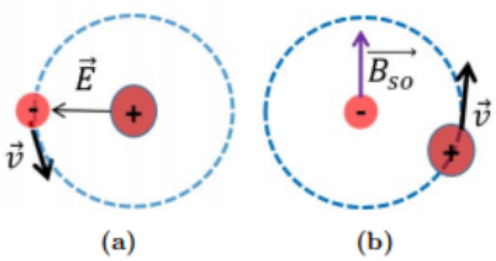

Figure 1.2 – Toy model for SOC. (a) Laboratory Referential. (b) Electron Referential. Adapted from Atoms, Molecules and Photons [5]

With the Equation 1.2, it is possible to estimate the energy changes due to the interaction of the electrons spin with the nucleus orbital magnetic field, $\Delta H_{SO} = \mu_\mathbf{s}.\mathbf{B_l}$, given by the Equation 1.3.

$$\Delta H_{SO} = \frac{\mu_0 Ze^2}{4\pi m_e^2 r^3}(\mathbf{s} \cdot \mathbf{l}) \tag{1.3}$$

The quantum analogous of this derivation may be obtained by perturbation theory. Here, the energy depends on the quantum numbers n, l and s. It is also possible to rewrite the energy in terms of the quantum number j, the total angular momentum. The general expression for the Spin-orbit coupling energy is given in Equation 1.4.

$$\Delta H_{SO}(n, j, l) = \frac{\alpha}{2}[j(j+1) - l(l+1) - s(s+1)] \tag{1.4}$$

In the above equation, α is the spin-orbit coupling constant and written as in Equation 1.5.

$$\alpha = \frac{\mu_0 Ze^2\hbar^2}{8\pi m_e^2 r^3} \tag{1.5}$$

Looking with a different approach to the spin-orbit interaction. The spin-orbit interaction strength λ increases rapidly with the atomic number Z. The dependence in a simple hidrogenic

model is well known and proportional to Z^4.The SO interaction of an electron in a central field of potential V (r) is given by:

$$H_{SO}(r) = \frac{1}{2m^2c^2}\frac{\partial V(r)}{\partial r}\vec{L}\cdot\vec{S} = \lambda(r)\vec{L}\cdot\vec{S} \tag{1.6}$$

If we evaluate this expression using the Coulomb potential $V(r) = -Ze^2/r$ and the hydrogenic wave functions $R_{nl}(r)$ with energy E^0_{nl}, we get perturbative correction due to the spin-orbit interaction:

$$E_{nl} = E^0_{nl} + \lambda_{nl} \times 2^{-1}[j(j+1)l(l+1) - s(s+1)] \tag{1.7}$$

where j and l are total and orbital angular momentum quantum numbers.

In this approach, we define the strength of the SOC λ_{nl} as:

$$\lambda_{nl} = \int_0^\infty R^2_{nl}\lambda(r)d^3r = \frac{\alpha^2_{fs}Z^4}{n^3l(l+1/2)(l+1)} \tag{1.8}$$

it's possible to observe that increases with Z^4, with α_{fs} being the fine-structure constant [50]. It is also important to emphasize that the SOC has a direct dependence of the electric potential which the electron is subject. The spin-orbit coupling induces changes in the atomic energy levels, known as fine structure [49].

In solids, the periodic arrangement of nuclei usually leads to a decrease of the SOC intensity. Then, the observation of a strong SOC in solids depend on symmetry considerations. The lack iof inversion symmetry is a condition to display considerable SOC.

SOC in solid systems can be classified in two types according to the form of inversion symmetry. If the system lacks an uni-axial inversion symmetry the SOC is known as Rashba-type. However, if the system does not possess an inversion symmetry center in the unit cell the SOC is known as Dresselhaus-type [51, 52]. The centro-symmetry breaking in a crystal structure introduces an additional terms in the SOC Hamiltonian of one electron. Such effect was firstly characterized by Dresselhaus [53] in zincblende structures. The interfacial inversion symmetry breaking was studied by Bychkov and Rashba [54]. This last type of SOC interaction leads to spin-dependent transport phenomena and will be one of the focused subject of our work.

One important consequence of SOC in magnetic solid systems is the connection between the crystal lattice and the magnetic moment direction, creating the preferred magnetization direction, known as the easy axis, rising to the magnetocrystalline anisotropy. This type of anisotropy is common in materials with large spin-orbit coupling [48]. In materials with lack

of inversion symmetry or bilayers of different materials, SOC can combine to the exchange interaction to generate an antisymmetric exchange interaction known as the Dzyaloshinskii-Moriya interaction (DMI) [19], [20]. This DMI can induce chiral ordering in the magnetic systems.

1.3 Rashba Spin-Orbit Coupling

The Rashba interaction term in the SOC energy arises from the broken inversion symmetry along a single direction of material structure. A typical system showing Rashba Spin-Orbit Coupling (RSOC) is the interface of two distinct materials, where a electrostatic potential asymmetry is induced and so an electric field is built. By using a simple toy model, it is possible to look to the potential asymmetry as a quantum well, as depicted in Figure 1.3. In this way, Vasko, Bychkov and Rashba [54] proposed that the existence of an electric field in z direction, perpendicular to a thin layer, results in an additional SOC term to the Hamiltonian [1], which is given by the Equation 1.9. A schematic of the toy model is presented in Figure 1.3.

$$\Delta H_{SO} = \mu_s.(\nabla V \times p) \tag{1.9}$$

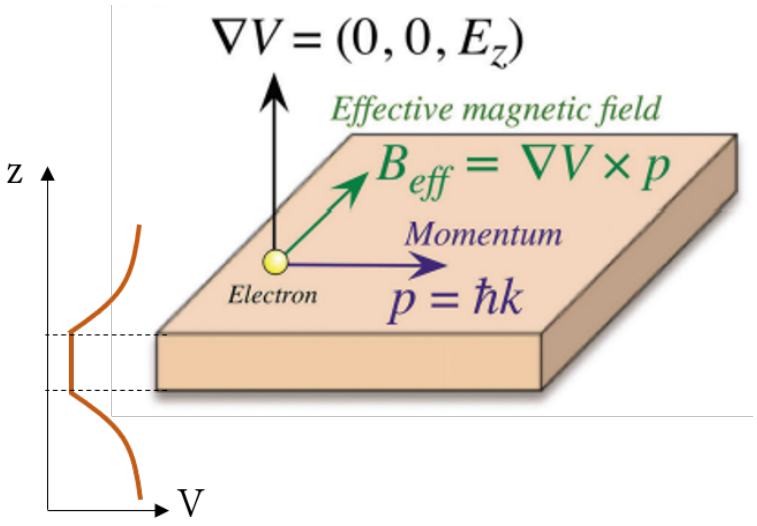

Figure 1.3 – Toy model for the Rashba effect in quantum wells. Adapted from ref [6]

Another usual treatment for the Rashba interaction comes from the nonrelativistic approximation to the Dirac's Equation [55]. In this form, the relation between the potential and the Rashba parameter is more explicit. Considering the Pauli matrices, a Coulomb potential and a

spinor representing the spin state up or down, after some mathematical manipulation [56], the spin-orbit Hamiltonian will be given by the Equation 1.10.

$$H_{SO} = \frac{\hbar^2}{4mc^2}\sigma \cdot (\vec{k} \times \nabla V) \tag{1.10}$$

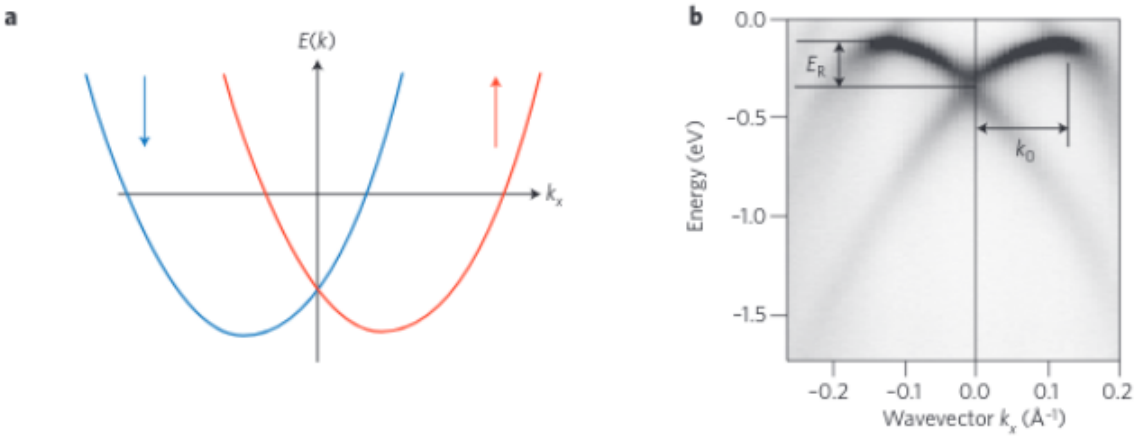

Figure 1.4 – (a) Schematic of the energy dispersion of a 1D free-electron gas with spin–momentum locking induced by Rashba spin–orbit coupling: the two bands carry opposite spin momenta, represented by the red and blue arrows. (b) Energy dispersion at the surface of a BiAg(111) alloy measured by ARPES, with energy shift ER and momentum offset k_0 being a clear indicator of Rashba splitting. ([1])

The term ∇V is the electric field induced by the broken inversion symmetry. For a quantum well along the z direction (electric field in z direction), Equation 1.10 may be written as:

$$H_{SO} = \frac{\hbar^2}{4mc^2}\nabla V_z \cdot (\sigma_x \vec{k}_y - \sigma_y \vec{k}_x) \tag{1.11}$$

In this form, the Rashba coupling parameter can be rewritten as

$$\sigma = \frac{\hbar^2}{4mc^2}\frac{\partial V}{\partial z} \tag{1.12}$$

As can be seen, this parameter is proportional to the potential gradient along the quantum well growth direction, i.e., to the electric field. The splitting of up and down spin bands in crystals due to Rashba effect can be well measured experimentally by using techniques such as ARPES (Angle Resolved Photo-Electron Spectroscopy), as shown in Figure 1.4b, for a quantum well formed at the surface of BiAg (111) [1]. Below, it is discussed some more manifestations of SOC in the case of transport properties of metals.

1.4 Magnetotransport

The Magnetoresistance (MR) is the modification of the electrical resistance by an applied magnetic field at a given constant temperature. The MR ratio can be described by the following expression, in Equation 1.13:

$$\frac{\delta\rho}{\rho} = \frac{\rho(H) - \rho(0)}{\rho(0)} \tag{1.13}$$

In Equation 1.13, $\rho(H)$ is the electrical resistivity in the presence of an applied magnetic field H and $\rho(0)$ represents the resistivity in the absence of magnetic field. For this work, the field is placed in different configurations relative to the current direction and sample plane. In thin films the current is established in the film plane, then there are three possible geometries, as it is shown in the Figure 1.5

The longitudinal magnetoresistivity ($\Delta\rho_{||}$) is measured in the configuration where the current and the magnetic field are parallel to each other, both laying in the film's plane, shown by the upper scheme in Figure 1.5. The transverse magnetoresistance ($\Delta\rho_{\perp}$) is obtained when field and current are perpendicular to each other, and both laying parallel to the film plane. Finally, the perpendicular magnetoresistance ($\Delta\rho_P$) is acquired when the field is applied perpendicular to the plane of the film, in a direction also perpendicular to the current. The perpendicular geometry is also called the Hall configuration.

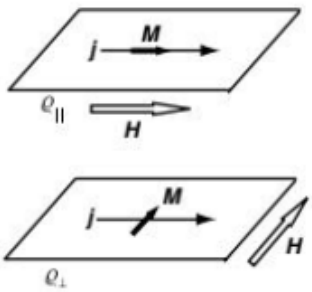

Figure 1.5 – Adapted from Magnetism and Magnetic Materials [4]. Up: schematic configuration for the longitudinal measurements. Down: schematic configuration for the transverse measurements.

The physical origin of magnetoresistance (MR) is due to several phenomena, depending on the electronic and structural properties of the system. In the case of metals the MR is usually

separated in two different forms: the ordinary and the anisotropic magnetoresistance [4], the first one occurs in all materials and is related to the orbitals degrees of freedom [57]. The second one is found in materials with magnetic behavior.

1.4.1 Ordinary Magnetoresistance (OMR)

The Ordinary Magnetoresistance (OMR), also called Lorentz Magnetoresistance [58], is a parabolic response to the applied field, where the electric resistance increases upon the argumentation of the field intensity according to an approximately parabolic law. This change in the electrical resistance of the material is due to the charge deflection of the free carriers, due to the Lorentz force in the presence of the magnetic field [47]. This type of magnetoresistance is usually present in both perpendicular and transverse geometry. However, it can be found in the longitudinal configuration although in smaller intensity.

The presence of the Lorentz force does not change the mechanisms of electronic scattering, but changes the momentum distribution of carriers, analogous to a change in trajectories of the free electrons. Such a deflection tends to put the charge carriers in a cyclotron orbit, which increases the electric resistance. This type of magnetoresistance is more prominent at low temperatures, once the mean free path and the mobility are higher. The Lorentz force is also responsible for the Ordinary Hall Effect, which will be discussed later in this work.

1.4.2 Anisotropic Magnetoresistance (AMR)

The Anisotropic Magnetoresistance (AMR) is usually found in ferromagnetic materials and depends on the orientation between the magnetization and current. Usually, in the longitudinal configuration, there is an increase in the resistance. The opposite occurs in the transverse orientation, whereas there is a decrease in the resistance by applying the field. The AMR Equation 1.14 is presented below [59]:

$$\frac{\Delta\rho}{\rho} = \frac{\rho_{||}(H) - \rho_{\perp}(H)}{\rho_{\perp}(H)} \tag{1.14}$$

The AMR is related to spin-orbit interaction, as it tends to mix current channels with opposite spins [4]. The effect is driven by the scattering of s- conduction electrons by d_{ϵ}- localized orbital, with ϵ spin component [60]. The magnitude of this effect can amount up to 3 percent of

resistivity value at zero field. In the Figure 1.6, it is possible to see the behavior of the electrical resistivity in both configurations, longitudinal and transversal, starting at zero magnetic field for an unmagnetized sample. The highest resistivity is found when the current flows parallel to the sample magnetization, while the lowest resistivity is found when the magnetization is perpendicular to the current. However, in some specific systems, such a half-metal, an inverse effect may occur [60]. It is important to understand that this effect is observed at low field, so the OMR and the AMR are hardly seen in the same range of magnetic field. The AMR effect can be observed in two different ways, one as oscillations in $\rho \times \theta$ curves, where θ is the angle between the current and the magnetic field, and second, in $\rho \times H$ curve, as symmetrical peaks at the coercive field, where there is an abrupt change in the sample magnetization.

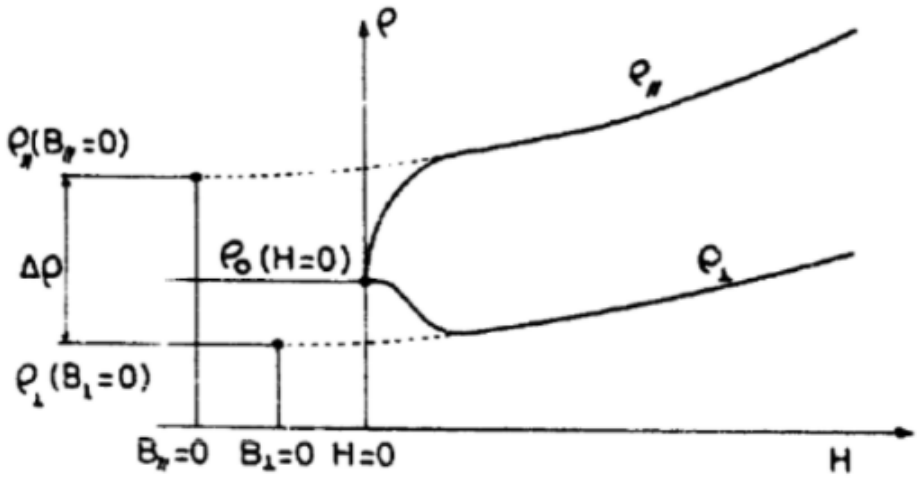

Figure 1.6 – Adapted from [7]. AMR representation, showing the magnetoresistance in longitudinal and transverse orientation. This effect can be defined as spontaneous anisotropy of resistivity

The AMR is related to spin-orbit interaction as can be seen in the expression below, of the CFJ Model (Fert-Campbell-Jaoul) [59].

$$\frac{\Delta\rho}{\rho} = \gamma(\alpha - 1) \tag{1.15}$$

where $\gamma = \frac{3}{4}(\lambda/H_{ex})^2$. The constant λ is directly related to the spin-orbit coupling. In this case, a variation in the spin-orbit interaction can be observed in the AMR results.

1.4.3 Hall Effect

At the end of the XIX century, Edwin H. Hall discovered what is now called the Hall effect [1]. This property of an induced transverse electric field created in a conductor when there is an electric current flowing perpendicular to an applied magnetic field [47, 57]. For a non-magnetic conductor the origin of this effect is the Lorentz Force, which deflects and accumulates the charges at the edges of the sample and creates an Electrical field E_y that balances the Lorentz force given by Equation 1.16:

$$\vec{F} = q(\vec{E} + \vec{v} \times \vec{B}) \tag{1.16}$$

The induction B_z is equal to $\mu_0 H_z$ in a non-magnetic material and v is the drift velocity of the carriers propagating as an eletric field current (J_x) produced by the longitudinal Electric field E_x. The force applied to the charge carrier generates a transverse electrical field (E_y), which is known as the Hall field, as it is shown in the figure below.

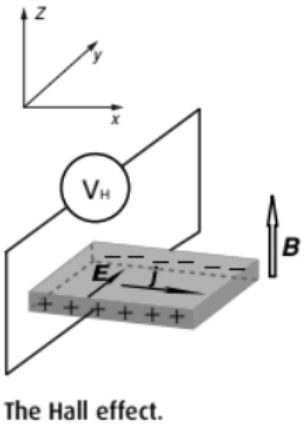

Figure 1.7 – Adapted from [4]. Configuration of Hall Effect measurement

Taking the transverse Electric field as $E_y = v \times B_z$ and current density as $J_x = nvq$, we obtain an expression for the Hall Field and consequently for the Hall Coefficient R_0 as follows:

$$E_y = \frac{1}{nq} J_x B_z = R_0 J_x \mu_0 H_z \tag{1.17}$$

where $B_z = \mu_0 H_z$, μ_0 is the vacuum permeability, and $R_0 = \frac{1}{nq}$ is the Ordinary Hall coefficient, which is associated to the charge density (qn). From the Equation 1.17, above, the

[1] Edwin Hall (1879), "On a New Action of the Magnet on Electric Currents"

Hall resistivity can be determined as given in Equation 1.18.

$$\rho_{Hall} = R_0 \mu_0 H_z \tag{1.18}$$

The experimental determination of R_0, allows one to obtain simultaneously the density and sign of the charge carriers ($R_0 < 0$ for electrons and $R_0 > 0$ for holes).

1.4.4 Anomalous Hall Effect (AHE)

The Hall effect, as described above, occurs in non-magnetic systems, as we derive the ordinary Hall effect only from the Lorentz force, meaning a purely orbital effect. In magnetic materials, the same Edwin H. Hall observed that this effect has much greater intensity [61]. In ferromagnetic materials, Hall observed a fast increase of the Hall resistivity for low applied magnetic fields and a linear field dependence in high applied fields. In 1893, Kundt noted that the saturation value of the Hall resistivity is roughly proportional to the magnetization M_z in ferromagnetic materials (Fe, Co, Ni) and has a weak anisotropy when the applied field is rotated with respect to the crystalline axis [8]. An empirical form for the Hall resistivity in magnetic materials, is given by [62, 63].

$$\rho_{xy} = \mu_0 R_0 H_z + \mu_0 R_s M_z \tag{1.19}$$

The second term, $\mu_0 R_s M_z$, represents the Anomalous Hall Effect (AHE) and R_s is the anomalous Hall coefficient. The fast increase in Hall resistivity by increasing the magnetic field is due to the AHE and reproduces the magnetization behavior towards saturation. The linear behavior at high magnetic field is due to the ordinary Hall effect. To experimentally determine the anomalous Hall coefficient, one can extrapolate the high field Hall resistivity to $H = 0$, as described in Equation 1.20 and shown in Figure 1.8.

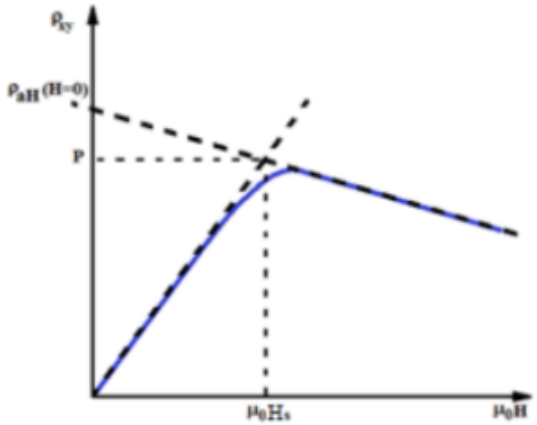

Figure 1.8 – Adapted from [7]. Hall resistivity as a function of the applied field. The dashed lines indicate the experimental method for analyzing AHE.

$$\rho_{AHE}(H=0) = \mu_0 R_s M_z \tag{1.20}$$

With this, we obtain the anomalous Hall coefficient as simple as in Equation 1.21:

$$R_s = \frac{\rho_{xy}(H \longrightarrow 0)}{\mu_0 M_z} \tag{1.21}$$

This anomalous Hall coefficient is related to different scattering mechanism such as: (i) intrinsic contribution, (ii) skrew-scattering and (iii) side jump. The first contribution, (i), was suggested by Karplus and Luttinger (1954) [64], they showed that when an external electric field is applied to a ferromagnetic solid, an additional contribution must be considered to carriers group velocity. In ferromagnetic materials the sum of this anomalous velocity contribution over all occupied bands can be nonzero, changing the Hall conductivity. This contribution, due to the band structure, receive the name of intrinsic contribution. This intrinsic contribution was recently related to a Berry phase in momentum space due to spin-orbit coupling.

Smit [65, 66] argued that another contribution to AHE is due to a skrew-scattering mechanism (i) from impurities in the solid lattice and related to the spin-orbit interaction. This mechanism presents a direct relation between the Hall resistivity (or anomalous Hall coefficient) and the sample longitudinal resistivity ($R_s \approx \rho_{xx}$). In the 70's, Berger [67] suggested the side jump experienced by quasiparticles upon scattering from spin-orbit coupled impurities also contribute to the AHE. This term was then understood as carrier wave-packet side jump caused by a scattering event by spin-orbit impurities. The Anomalous Hall coefficient in this mechanism is proportional to the square value of the longitudinal resistivity ($R_s \approx \rho_{xx}^2$). This is the same

relation obtained by the intrinsic contribution, so further analysis is necessary to separate these two effects. In the Figure 1.9 above, the three mechanisms are

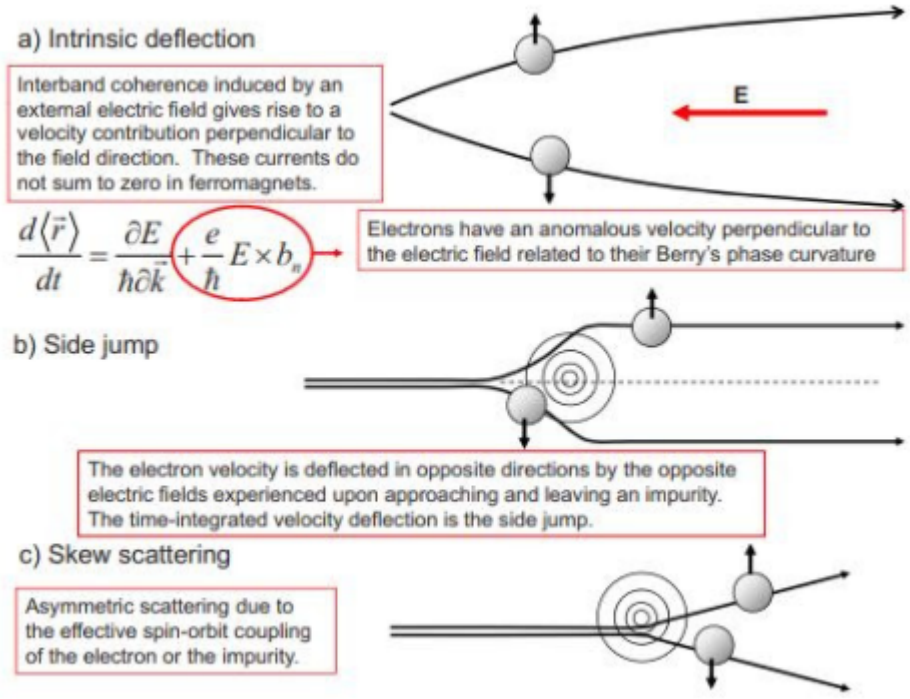

Figure 1.9 – Adapted from [8]. Schematics for the main AHE scattering mechanisms.

Taking into account the three mechanisms discussed above, it is possible to write the Anomalous Hall Coefficient as given in Equation 1.22:

$$R_s = A\rho_{xx0} + B\rho_{xx}^2 \tag{1.22}$$

Where ρ_{xx0} is the residual resistivity. To differentiate the intrinsic and the side-jump mechanism, we can write A,as in Equation 1.23:

$$A = A' + b\rho_{xx0} \tag{1.23}$$

Now the three different contributions are separated. The $A'\rho_{xx0}$ is the extrinsic contribution due to the skrew-scattering and the $b\rho_{xx0}^2$ is due to the side jump, which is also an extrinsic term.The third term in Equation 1.22 is the intrinsic AHE contribution, which is proportional to the square of the total longitudinal resistivity.

1.5 Transport in Ferromagnetic Materials

In metals, the resistivity can be modeled as a function of temperature by the Matthiessen Rule, in two addictive terms. The first term represents the residual resistivity, contribution from static defects in the crystalline structure. The second term has a dependence with the temperature, it is related to ideal carrier scattering mechanisms, such as those produced by phonons, electrons, spins, etc. In the simplest case of a non-magnetic metal with non-correlated electrons, the temperature dependent scattering is mainly due to carrier interaction with phonos,so that the Matthiesen's rule may be writen as the Equation 1.24.

$$\rho_{metal} = A\rho_0 + \rho_{pho}(T) \tag{1.24}$$

In magnetic materials, another term must be added to the expression above, related to the scattering of the conduction electrons by magneticexcitations. Since the Matthiessen rule [4] remains valid, this third term also has a dependence with the temperature, and the resistivity can be written as in Equation 1.25

$$\rho_{metal} = A\rho_0 + \rho_{pho}(T) + \rho_{SM}(T) \tag{1.25}$$

At high temperatures, the term $\rho_{SM}(T)$ is constant and attributed to the spin disorder. At low temperatures, this term is related to carriers scattering by magnons. For materials with strong SOC, another term can be considered. It is related to the interaction of the spin (of free carriers) at the conduction band with the orbital motions of the localized electrons, as shown in Equation 1.26.

$$\rho_{metal} = A\rho_0 + \rho_{pho}(T) + \rho_{SM}(T) + \rho_{S-O}(T) \tag{1.26}$$

Usually, a generalized form to write the resistivity is in the form of a power-law of temperature as in the Equation 1.27 below:

$$\rho_m = \rho_0 + \alpha T^{\beta} \tag{1.27}$$

In the above equation, the β is an exponent related to different mechanisms. In the low temperature limit, β equals to 5, is associated with the electron-phonon (acoustic) interaction. In cases with s-d phonon scattering, $\beta = 3$. For cases with electron-electron scattering, $\beta = 2$. For ferromagnetic materials, the electron-magnon scattering also corresponds to $\beta = 2$

2 Experimental Methods

In this chapter, we present the experimental techniques used to prepare the samples and to obtain the results of this work. The samples were prepared by using Magnetron Sputtering Deposition technique. For the characterization of the samples, we have applied X-Ray Diffraction (XRD), Rutherford Backscattering Spectroscopy (RBS) and Vibrating Sample Magnetometer (VSM), the last one for the characterization of magnetic properties. Finally, we have used electrical transport techniques to measure electrical resistivity, magnetoresistance and Hall effect, in the temperature range of 1.8 to 300 K.

2.1 Samples Fabrication by Magnetron Sputtering

All samples presented in this work were fabricated by using a Homemade Magnetron Sputtering system at the Laboratory of Magnetism (LAM- UFRGS). In the Magnetron Sputtering process, the chamber has its pressure reduced to a lowest value, known as base pressure, here this value is about 2×10^{-7} Torr. For this, a set of vacuum pumps (root, diffusion and criogenic pump) were applied. After the lowest pressure being attained, a constant flux of Argon (about 200 sccm) is introduced inside the chamber, increasing the pressure to about 1 mTorr, which is the working pressure. A voltage drop is applied between the target (made from the material to be deposited) and a counter-electrode, just above the target, building up an electric field, which ionize the Argon gas. The target is grounded and the upside counter-electrode is positively charged. The Argon generate a plasma that is stabilized by the continuous collisions of the neutral gas with the electrons trapped close to the target by strong magnets. Then, the ions of Ar^{+} are accelerated towards the target, leading to high energy collisions. The atoms at the surface are ejected into the environment with energy enough to reach the substrate, condensing and depositing a thin films. The equipment used in this work has five deposition guns; the sample holder (where the substrate lays down) is positioned at about 15 cm above the targets. Two sources, one DC and another RF were used. The equipment also contains three different pressure gauges, monitoring the chamber, diffusion and root pump pressure environments. Figure 2.1 shows a scheme of the Magnetron Sputtering deposition system. The presence of magnets in the base of the sputter gun confine the plasma near to the target enhancing the sputter process and allowing a smaller working pressures

[9].

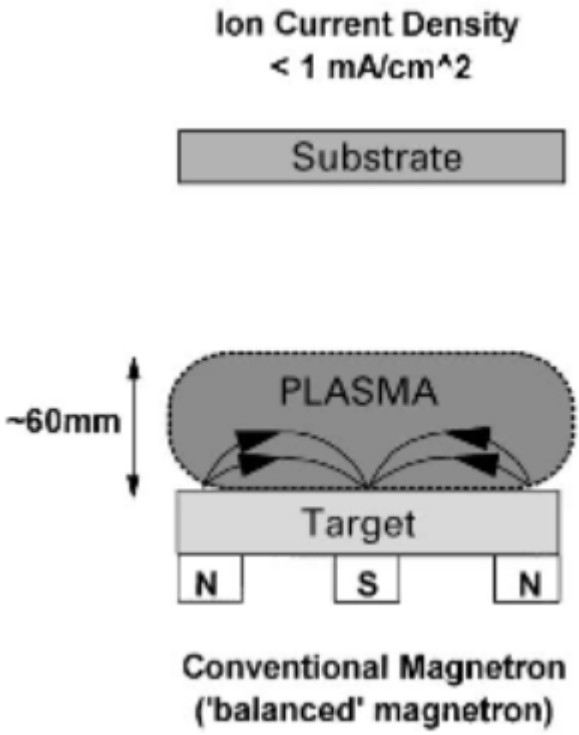

Figure 2.1 – Adapted from [9]. Schematic figure of a magnetron sputtering deposition system.

With a fixed set of parameters, i.e. pressure, Ar flux and potential applied at the DC and RF guns, we calibrated the deposition rates for the metals used in this work (Cobalt, Bismuth and Titanium). Additionally, we mapped the deposition homogeneity along the sample holder, it was observed about 10-15 $\%$ thickness deviation along the 3 inches (diameter) sample holder. For the samples prepared in this work, the substrate was a very flat $SiO_2(100nm)/Si$ wafer.

In this work, thin layers of Cobalt and Bismuth were deposited alternately with 10 times repetitions, forming a heterostructure. The prepared samples have the following structure $Si/SiO_2/(Co(x)Bi(y)) \times 10/Ti(2nm)$, with x = 0.5; 0.75; 1 and 2, while the y = 1 and 3. The Ti were used as a capping layer, preventing the oxidation of the overall structure. As reference samples, we also prepared thin films of pure Bi(30nm) and Co(20 nm and 10 nm).

2.2 X-Ray Diffraction (XRD)

For the characterization of the crystalline structure of the multilayers, we have employed X-Ray Diffraction (XRD) analysis, by using a Bruker D80 diffractometer (Laboratory of Nanoconformation -LCN- at Physics Institute of UFRGS) with CuK_α radiation (1.5422 A), in

both, the $\theta - 2\theta$ configuration (Bragg–Brentano goniometer) and in the Grazing Angle Incidence X-Ray Diffraction (GIXRD) configuration. XRD is one of the most powerful techniques to understand the crystalline structure of solids, giving information about grain size, preferential growth orientation and possibly chemical analysis. In this technique, the X-Ray beam is focused on the sample. The reflections over distinct parallel crystalline planes generates a diffraction pattern which is a characteristic pattern of each crystalline structure. The X-Ray is used because of the wavelength size (0.5 to 2Å) close to the lattice parameters of the solids [68], allowing the diffraction phenomena. It is possible to relate the distances between the crystal planes with the wavelength of the X-Ray radiation and the 2θ angle where a constructive interference take place, accordingly to the Bragg´s law, as indicated in the Equation 2.1. Using the Bragg-Brentano geometry, presented in Figure 2.2, the diffraction pattern of the crystals planes parallel to the substrate surface can be obtained.

$$n\lambda = 2d_{hkl}sin\theta \tag{2.1}$$

We use this data to understand the crystalline trends of the samples, searching for possible mixed phases and crystalline textures in the grown samples.

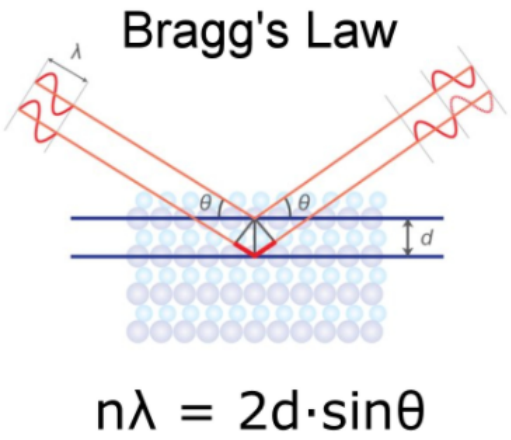

Figure 2.2 – Schematic figure of XRD in Bragg-Brentano Configuration. Adapted from [10].

2.3 Rutherford Backscattering Spectrometry (RBS)

The Rutherford Backscattering Spectrometry (RBS) is an analysis technique often applied in the characterization of thin films. RBS consists of shooting the sample with a mono-energetic incident beam of alpha particles (He^{+2}). After this process, the backscattered particles are

detected by a Silicon detector which is positioned at an angle of 165° from the incident beam. This signal is processed, amplified and converted into counts by energy channels. Figure 2.3 shows the scheme of a RBS chamber. The backscattered alpha particles have intensity and energy dependent on the target molar mass and density [69].

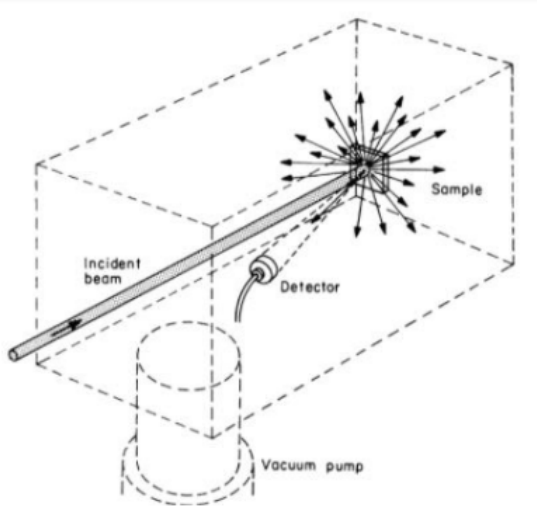

Figure 2.3 – Adapted from [11]. Schematic figure of RBS

In the Figure 2.4 is presented a RBS spectrum. In the x-axis is the energy channel and in the y-axis is the intensity of counts. The channel-to-energy calibration is done by using a material with a known kinetic factor (relation between the incident energy and scattered energy at a given angle), such as Au (0.9232), so one can determine energy correspondence to each channel.

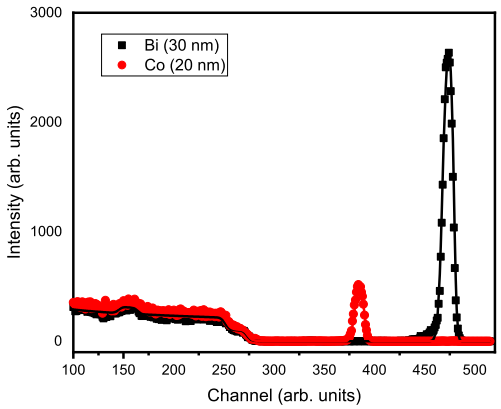

Figure 2.4 – RBS data for thin film of Co and Bi

In the Figure 2.4, the black data is the RBS for a sample with 30 nm of bismuth over the SiO_2 substrate. The peak at about the channel 470 are the alpha particles scattered by the Bi atoms. The area of the peak is related to thin thickness, given a areal atomic density of about

$120 \times 10^{15}\ atm/cm^2$. The signal below the channel 275 is due to the SiO_2/Si substrate, which is very thick. The right rising edge of the peak depends essentially on the target material, while the area of the peak depends on the sample thickness and composition. The analysis is done by simulating the curves in the software SIMNRA [70]. The red curve is the same analysis for a thin films of Co with the areal atomic density of $170 \times 10^{15}\ atm/cm^2$.

In our work, the spectrum were obtained using a TANDEN HVE particle accelerator with 3 MeV. This equipment is located at the Laboratory of Ion Implanting - Institute of Physics of UFRGS. All the RBS measurements were done using a 1.5 MeV alpha beam.

2.4 Magnetic Characterization - Vibrating Sample Magnetometer

All the magnetization measurements in this work, including M x H and M x T analysis, were done in a Vibrating Sample Magnetometer (VSM). The VSM, created by Simon Foner [71], is a versatile tool to characterize magnetic samples. A vertical vibration head is connected to a rod which holds the magnetic sample. The sample is then placed upon a magnetic horizontal field, created by an electromagnet. Four pick-up coils are placed in between the sample and the poles of the magnet. The magnetic flux of the vibrating samples can be detected by the pick-up coils and is proportional to the sample magnetization. The voltage induced in the pick-up coils is transmitted to a lock-in amplifier, which is tuned at the same frequency as the sample vibration. Attached to the electromagnet there is a current source that controls the magnetic field applied through the sample, changing its magnetization. This equipment can be used to study different magnetic properties, like Coercive Field, saturation magnetization and hysteresis [72]. Figure 2.5 displays a scheme of the VSM setup.

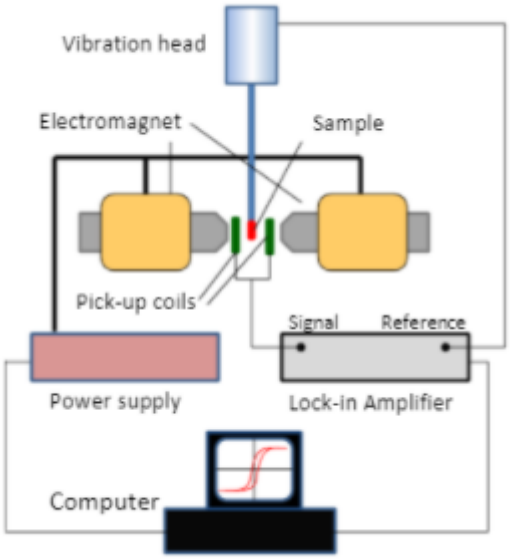

Figure 2.5 – VSM measuring functional scheme [12]

Here, we have used the VSM model EZ9 from MicroSense Company, installed in LAM of the Institute of Physics of UFRGS. This equipment is able to measure magnetic moment with a sensitivity down to 10^{-6} emu and apply magnetic field up to 22 kOe.

2.5 Electrical Characterization

2.5.1 DC Resistivity

The electrical resistivity of the samples were measured by using a DC electrical current. All the samples were electrically connected by using 0.25 mm diameter copper wires, attached to the sample with cryogenic silver paste. We have used the 4-probes method, in which is possible to apply a steady current (two points) through the sample and measure the voltage drop over two other distinct electrodes. The main advantage of the 4-probe method is the possibility of measuring the sample electrical resistance without contribution of wires and contact resistance. In Figure 2.6 is displayed the electrical contacts structure: The voltage channels (indexed as a or b) were used for magnetoresistance measurements, while the voltage electrodes V_{b+} and V_{a+} or V_{b-} and V_{a-} were used for Hall measurements.

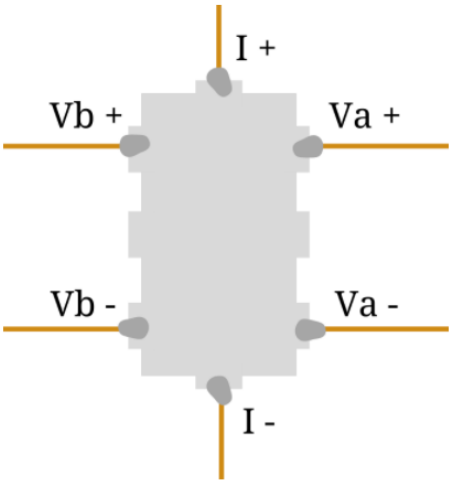

Figure 2.6 – Schematic sample measuring points. The I terminals represent the points connected to a DC current font and define the current flux. The V terminals represent the voltage reading connected to a voltmeter.

The samples were attached to a sample holder and inserted into the cryogenic chamber at low temperatures. The R x T measurements and Hall effect measurements were performed using the 9 Tesla C-Mag Cryostat (Cryomagnetics, Inc), working in the range of 1.8 K to 300 K. The Magnetoresistance measurements were done by using a DE-202N axially symmetrical Cryostat (ASRCryo), working between 25 K and 300 K.

2.5.2 Magnetoresistance Measurements

The magnetoresistance in the multilayered samples were measured in three different configurations, related to the current and magnetic field directions, as depicted in 2.7. The three configurations used here are known as longitudinal, transverse and perpendicular.

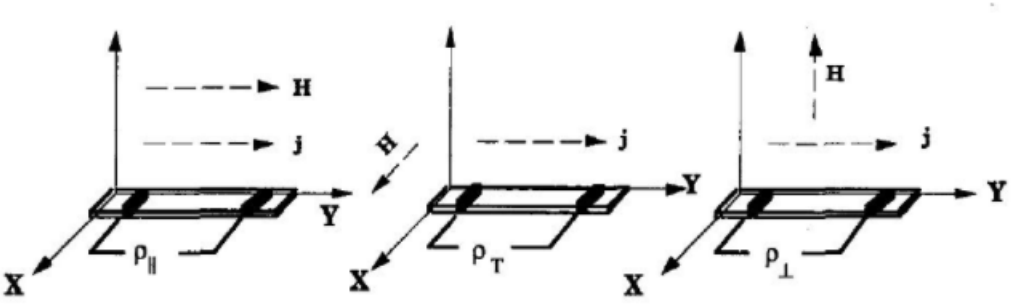

Figure 2.7 – Different magnetoresistance measurements configurations [4]. From left to right, longitudinal, transverse and perpendicular.

In the longitudinal (LMR) configuration, the applied field (H) is parallel to the current (J). In the transversal (TMR) configuration, the field is applied in the same plane of the current

(sample plane), but in a perpendicular direction. At last, the perpendicular configuration (PMR), also known as Hall configuration, is when the applied field goes through the sample plane, which is also perpendicular to the current. So, it is possible to measure three different magnetoresistances ($\Delta\rho$), as defined by the experiment configuration. During the measurement, the resistance of the sample is adquired continuously while the magnetic field sweeps. The LMR and TMR were measured from -2 kOe to 2 kOe, while the PMR was measured from -50 kOe to 50 kOe.

2.5.3 Hall Effect

For the measurement of the Hall resistivity, we have used the Hall cross sample geometry (shown in the Figure 2.8) in order to minimize any magnetoresistance contribution. The voltmeter was attached in opposite points of the sample in a perpendicular position relative to the current terminals. The magnetic field is applied perpendicularly to the sample plane. In these measurements the magnetic field is generated by using a superconductor coil reaching up to 90 kOe. The samples shape were patterned by using a shadow mask during the deposition.

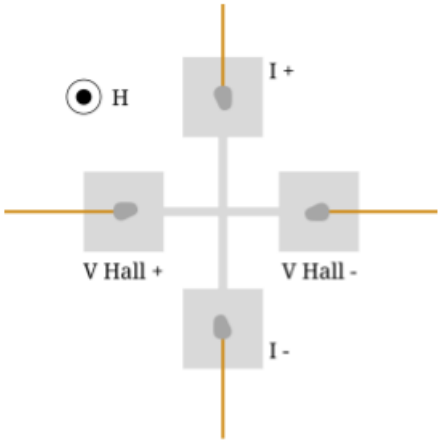

Figure 2.8 – Hall sample scheme measurement

3 Preparation and Characterization of the Samples

In this chapter is given a detailed description of the samples used in the present work, with focus on the structural and magnetic characterization.

3.1 Sample Structure

Samples were deposited on $SiO_2(100nm)/Si$ wafers using Magnetron Sputtering. The depositions were performed with the following parameters: Base Pressure of 2×10^{-7} Torr, Working Pressure of 1×10^{-3} Torr and Argon flux of 200 sccm. A RF power source was used for Cobalt deposition, with power of 45 W and a DC source for the Bismuth at power of 10 W. Thin Cobalt and Bismuth multilayers were deposited alternately with 10 times repetitions, varying thickness from 0.5 to 3nm (x and y), fabricating samples with the follow stacking $Si/SiO_2Co(x)Bi(y)x10/Ti(2nm)$. We adopted the nomenclature Co(2)Bi(3) for a sample with 10 layers of Cobalt 2 nm thick, deposited alternately with 10 layers of Bismuth with thickness of 3 nm, Figure 3.1 shows a schematics of the multilayered samples. All the samples have an additional capping layer of Titanium to prevent degradation. Thin films of Bi(30 nm), Co(10 nm) and Co(20 nm) were also prepared as reference samples.

In order to check the layer thicknesses and composition we have used RBS analysis with the software SIMNRA [70] (for the data processing). The results are presented in the Figure 3.2 and the data from the fitted curves is resumed in the Table 3.1.

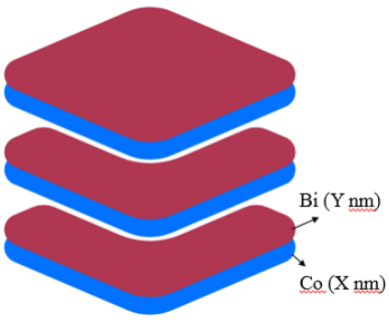

Figure 3.1 – Schematic structure of multilayers with the 3 repetitions of bilayers

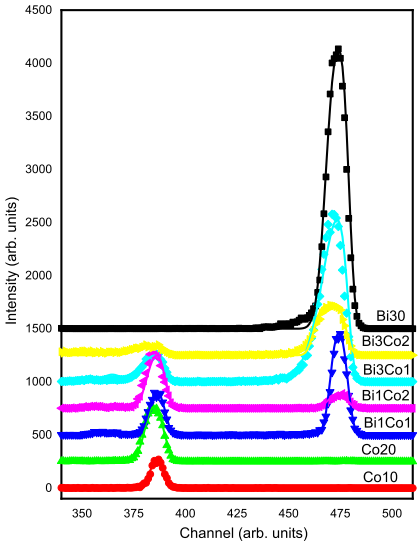

Figure 3.2 – Resumed RBS data of the studied samples. All the SiO_2 curves are ajusted and supressed

The conversion from SIMNRA thicknesses given in $atom/cm^2$, to thickness in nanometer, were done by assuming bulk mass densities for the layers, i.e., $\rho_{Co} = 8,9 g/cm^3$ for Cobalt and $\rho_{Bi} = 9,8 g/cm^3$ for Bismuth. We know that such assumptions are not really accurate for thin films, where usually a slightly smaller mass density is observed, in comparison to the bulk. The data from RBS simulations, nonetheless, are close to the values expected (from previous calibrations). For instance, in the sample Co(1)Bi(1), the RBS analysis furnishes about 1,1 nm of Co and 1,0 nm of Bi. The RBS analysis served as a benchmark to confirm the specifications of the samples

Table 3.1 – Parameters obtained from the fit of RBS data using the software SIMNRA

Sample	**Thickness** ($\times 10^{15}$**atm/cm²**)	**Thickness (nm)**
Co (10nm)	124	13.6
Co (20nm)	171	18.8
Bi (30nm)	119	42.3
Co(1)Bi(1)	10.2 / 2.8	1.1 / 1.0
Co(2)Bi(1)	16.5 / 0.51	1.8 / 0.2
Co(1)Bi(3)	10.4 / 7.6	1.1 / 2.7
Co(2)Bi(3)	13.9 / 8.1	1.6 / 2.9

In the Figure 3.3 is presented the RBS spectrum of the sample Co(1)Bi(1), where the numerical simulation of the spectrum fits very well the experimental data. To obtain good fitting in thicker samples, such as Co(2)Bi(3), roughness was added to the simulation.

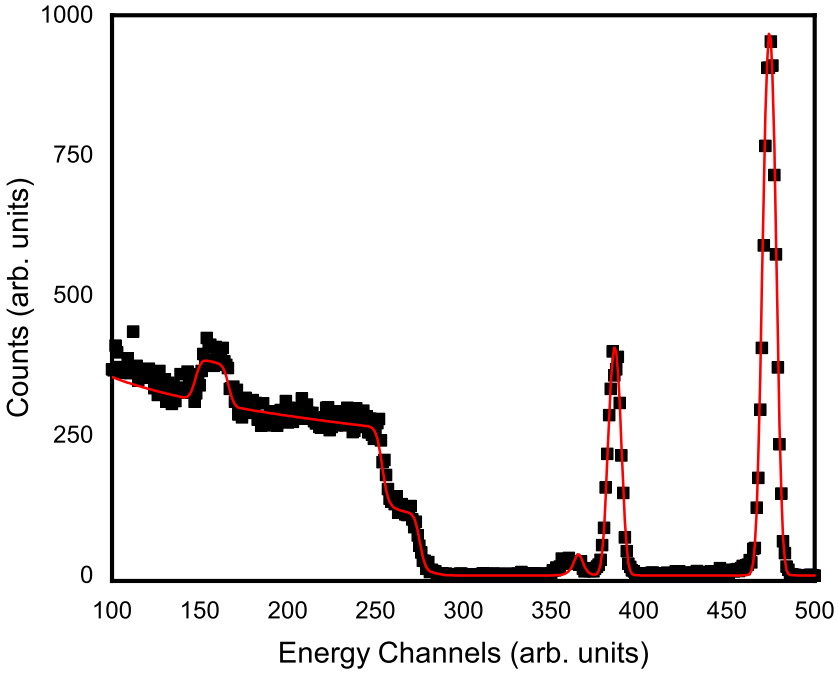

Figure 3.3 – Co(2)Bi(3) data adjusted with software SIMNRA. The red dots are the counts in different channels of RBS. The red line is the simulation to adjust the data.

With the RBS data, we try to search evidences for uniform stacking of layers. We compare the simulation of both multilayer stacking and the simulation of a compound of Bismuth and Cobalt (mixed Co and Bi). In the Figure 3.4, it is shown the data for both cases. By comparing the two simulations, no differences in the spectra were found, meaning that the RBS analysis do not have enough precision to resolve between those two layer configurations. We point out, however, that a mixture of Co and Bi in atomic level is rather improbable, given the small interdiffusion between these two atoms. Additionally, the compound $CoBi_3$ has been obtained only in high pressure and high temperature conditions [73].

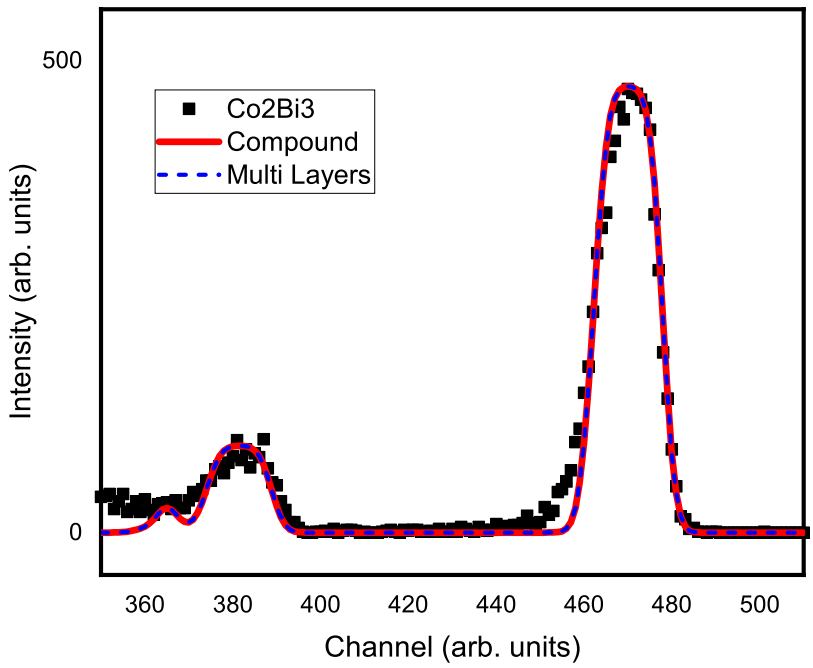

Figure 3.4 – Co(1)Bi(1) data adjusted for multilayer and compound. The black dots are the experimental data. The blue dashed line is the multilayer simulation and the red line is the compound simulation. No roughness was used in these simulations.

3.2 Crystalline Structure

The crystalline structures of the samples were probed by X-Ray Diffraction. The results are displayed in the Figure 3.5, showing the pattern for the reference samples Bi and Co along with the pattern of the sample Co(2)Bi(3). The XRD pattern indicates a crystallographic texture for the Bismuth reference sample, along [001] basal planes, as indicated by the high intensity of the peak at about 22°, from (001) Bismuth planes, compared to the peak at 27° from (012) planes. However, such texture is not observed in the Bi/Co multilayer, which presents mostly a powder pattern. The pattern for the Co reference sample, is shown in the Figure 3.5 in green, multiplied by 50 in order to fit the scale. It shows that the 20 nm Cobalt layer is probably a mixture of an amorphous phase, with some portion of crystalline grains. The evidence of the amorphous phase is the broad background under the peaks at 44.8° and 47.6°, both peaks from the hexagonal - HCP phase of cobalt (space group $P6_3/mmc$). Amorphous cobalt thin films grown on silicon have been previous reported [74] as well as, a mixture of amorphous and crystalline phases [75]. The vertical lines in Figure3.5 indicate the position and intensity expected for the Bismuth

($R-3m$) and Cobalt ($Fm-3m$ and $P6_3/mmc$) phases.

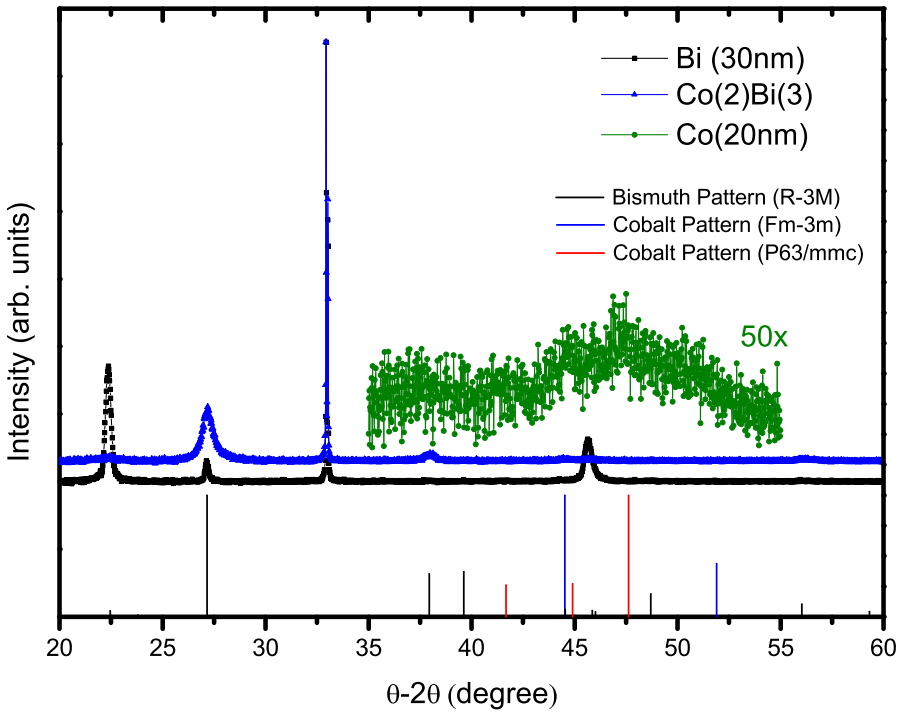

Figure 3.5 – XRD data for pure Cobalt with 20 nm thickness (green data), pure Bismuth with 30nm (black data) and multilayer of Co(2)Bi(3) (blue data). The peak not indexed in the graph is due to Silicon substrate.

In the Figure 3.6 is presented a zoom of the XRD pattern for the sample Co(2)Bi(3) along with the pattern from reference Co samples, in the range of 40° to 54°. One can see that the peak at 44.9°, from (002) basal planes, increases its intensity while the peak at 47.6°, from the planes (101), decreases. This last data could indicate the presence of texture in the Co layers, such as a preferential growth direction that could be related to the presence of Bismuth. Notice that the amorphous background also disappear in Co(2)Bi(3), indicating a better crystal structure, with less defects and grains boundaries. Many buffer layers have been used to enhance the cobalt crystallinity and texture, e.g. Tantalum [76]. The peak at 45.9° is from Bismuth layers, due to the (006) diffraction. The vertical lines in the bottom of Figure3.6 display the position and intensity of peak from HCP Cobalt.

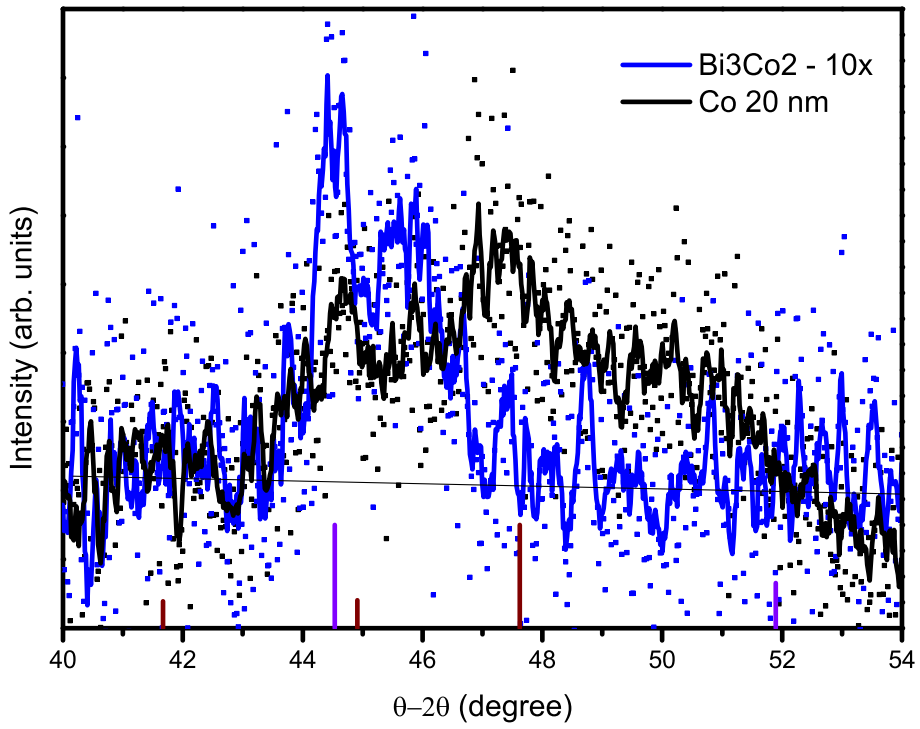

Figure 3.6 – XRD data for pure Cobalt with 20 nm thickness (black data) and multilayer of Co(2)Bi(3).

3.3 Magnetic Characterization

Magnetization measurements were used to support the structural and morphological results. The analysis were separated in two different lines. First, to understand the magnetic behavior of cobalt layers over the multilayers. It is important to remember that Cobalt is a Ferromagnetic material (FM) and Bismuth is a strong diamagnetic material. Second, we wish to understand the anisotropies of Cobalt layers and how its relates to the structure and the morphology of the samples.

Hysteresis ($M \times H$) loops for all the samples studied here are presented in the Figure 3.7. The data shows only the FM contribution from cobalt layers. The diamagnetic contribution from Bismuth is removed, together with the diamagnetism from the sample holder, by subtracting a linear term, observed at high magnetic field (H > 10 kOe). From the data, one can clearly observe three groups of samples related to the Cobalt thickness: with 0.5 nm, 1 nm and 2 nm per bilayer repetition. This data confirms the quality of the prepared samples. Many other features can be seen, such as: an increase of coercive field by reducing the Co thickness and by increasing the Bi

thickness. These characteristics will be discussed in teh next chapter.

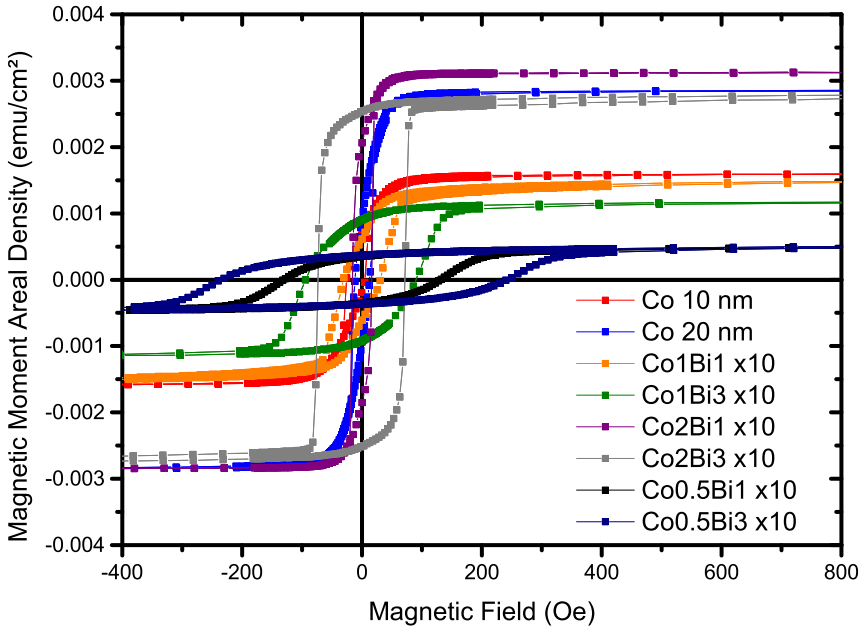

Figure 3.7 – Magnetization vs. Magnetic Field for the studied samples.

Figure 3.8 shows an hysteresis curve measured at room temperature (RT) in the field range of -20 kOe to 20 kOe, for the sample Co(2)Bi(3). In the graph two curves are shown. In black, the x-component of the magnetization, also named in-field, that is parallel to the applied magnetic field (also in x-direction). In red the y-component, also named out-field, which is the magnetization measured perpendicular to the field. The sample is positioned in the sample holder in a way that the y-axis is parallel to the substrate normal direction, i.e., the y-axis is perpendicular to the sample plane. The black data shows an usual behavior of a ferromagnetic material, with coercive field of about 80 Oe and remanence at about 90% of the saturation magnetization. The red curve do not shows any magnetization, meaning that no magnetic moment rotate out of the sample plane during the magnetization reversal. Such results point out to the high in-plane anisotropy of the samples.

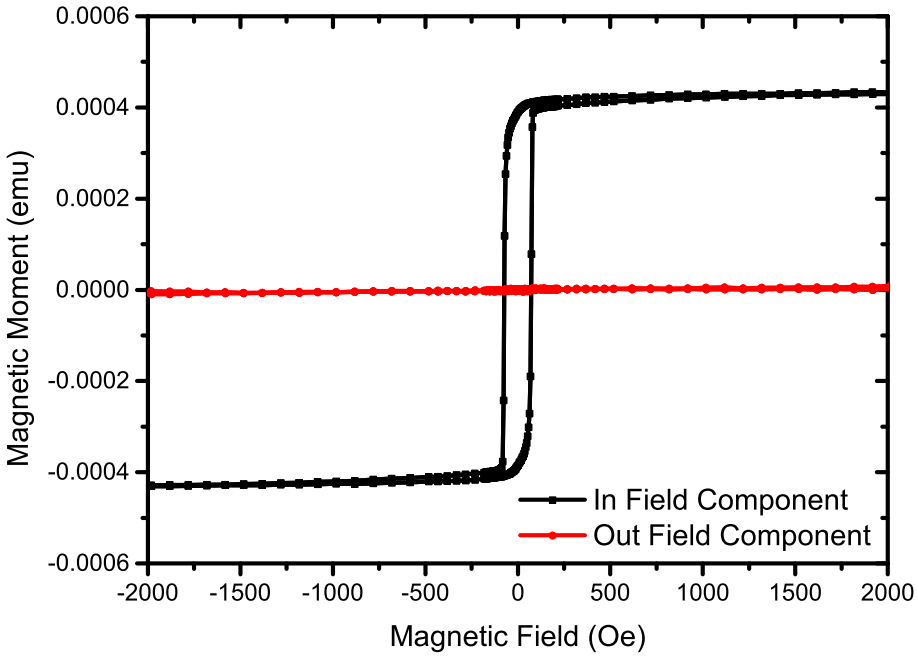

Figure 3.8 – Magnetization vs. Magnetic Field for Co(2)Bi(3) sample in the x direction (parallel to the applied field) and the y direction (perpendicular to the applied field).

Figure 3.9 shows the in-field magnetization for the same sample, but in two different configuration. The red circles are data obtained when the magnetic field lays in the sample plane (known as in-plane field). The black squares represent the magnetization data for the field going in the plane of the sample, i.e., the out-of-plane magnetization. The large hysteresis in the out-of-plane configuration is probably related to the high demagnetization field over the sample. The large saturation field, meaning a small FM susceptibility, could be described as consequence of high in-plane anisotropy of the sample, as described by the Stoner model [4]. Such results point to a flat structure for the cobalt layers. It rules out possibility for an uniform mixture of Co and Bi in the multilayers or even the presence of isotropic Cobalt clusters, in which we shall not expect such in-plane anisotropy.

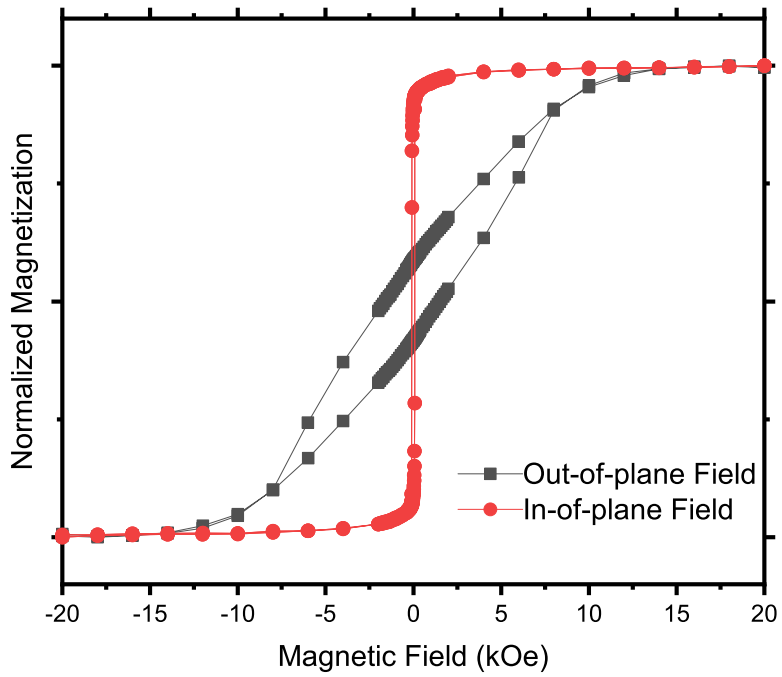

Figure 3.9 – Magnetization vs. Magnetic Field for the Co(2)Bi(3) sample in the in-plane configuration and out-plane configuration.

The in-field in-plane magnetization curves for the Co(2)Bi(3) with the magnetic field pointing in different directions over the sample plane (magnetic field rotating in the plane) are presented in Figure 3.10. It is seen that the coercive field, remanent magnetization and the area enclosed in the hysteresis changes with the angle. It means that there is also a small anisotropy in the sample plane as well, which is possibly related to an uniaxial domain structure of the magnetic domains. Such an uniaxial domains could be induced during the deposition process where some residual field from sputtering gun should be present [77]. The easy axis is the one showing high coercive field and high remanent magnetization, i.e., at 0° [4].

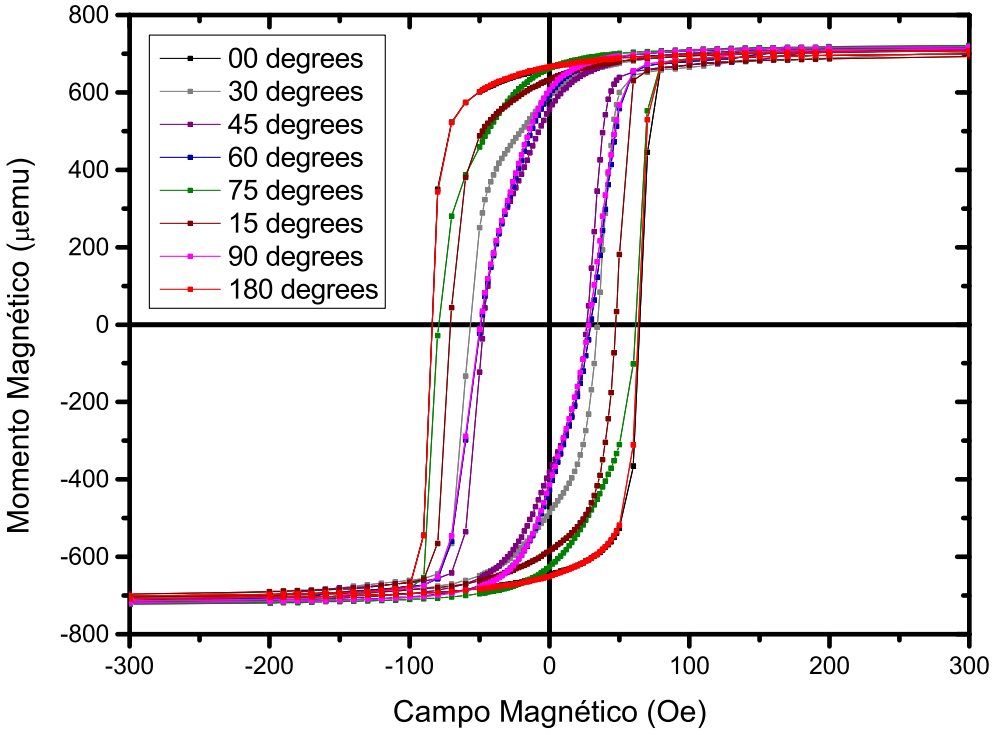

Figure 3.10 – Magnetization vs. Magnetic Field for Co(2)Bi(3) sample at different in-plane angles.

4 Results

In this chapter, we describe the main results based in magnetic and magneto-transport experiments. First, the magnetic properties of the multilayer will be discussed, such as the increase of coercive field of the samples, which could be related to the DM interaction at the Bi/Co interface. Then, the magnetoelectrical properties induced by the stacking. We found out an overall enhancement of the magnetoresistance and anomalous Hall coefficient, which could be related to the increase of the spin-orbit coupling in the Co layer near to the interface with Bismuth. All this results will be addressed below.

4.1 Magnetic Properties of the Multilayers

4.1.1 Magnetization vs. Temperature

The magnetization as a function of temperature was measured in the VSM system, as described in Section 2.4. The temperature range of the measurements was from 80 K to 300 K, by using liquid nitrogen cooling. The measurement procedure was the following: The desired measuring temperature was set. After waiting some for equilibration, a field sweep from -20 to 0 KOe was applied, and the magnetization measured simultaneously with the field sweeping. The saturation magnetization(M_{sat}) was obtained by extrapolating the magnetization curve (a straight line) till y-axis, where the field is null. Figure 4.1 illustrates this procedure. The remanent magnetization (M_{rem}) is obtained by taking the magnetization extrapolated to zero magnetic field. This procedure is important to remove the magnetization contribution due to the quartz sample holder and silicon substrate, both presenting diamagnetism.

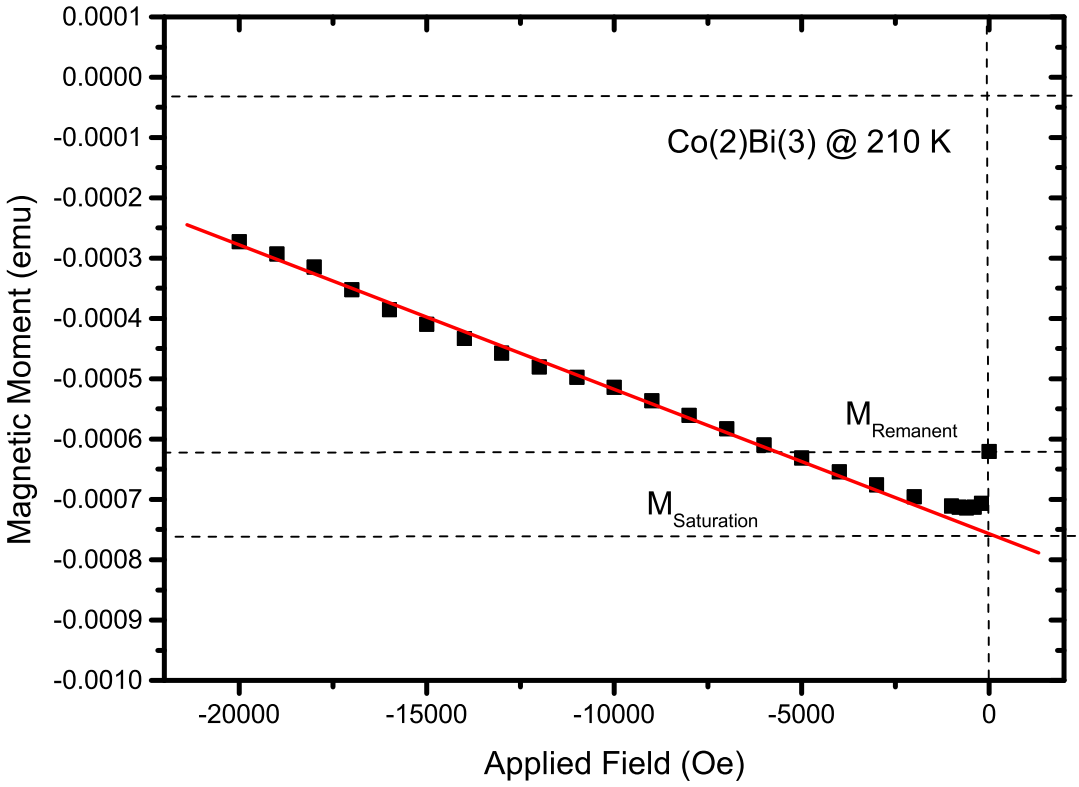

Figure 4.1 – M vs. H curve and the methodology to extract M_{sat} and M_{rem}.

The saturation magnetization of the samples are presented in the Figure 4.2. The data are normalized by the $M_{sat}(T = 0)$ (which is obtained by fitting chosen functions to the data as explained below) and multiplied by the cobalt layers thickness, in order to separate and highlight the data from distinct samples. Equation 4.1, which is usually referred as Bloch Law [57, 78] is used to fit the data. In this equation, the exponent *n* usually assumes the value 1.5, the T_{Curie} is the Curie temperature and the $M_{sat}(T = 0)$ is the saturation magnetization at 0 K. However, for nanostructures and thin films it can be, as higher as, 3 [78]. In the Figure 4.2 are displayed the data obtained from five samples, with distinct cobalt thicknesses. For each samples two fittings were done, one with the coefficient $n = 3/2$ (dashed line) and another with $n = 3$ (dotted line). Independently of the used fitting function, it is clear that the measured data is in the saturated temperature regime, i.e., for any temperature lower than 80 K, the saturation magnetization should remain almost constant. The Curie temperature can not be precisely determined by the fittings, once there are no data measured in temperatures close to the FM transition. However, some features should be pointed out. (i) The Curie temperature obtained with the $n = 3/2$ exponent gives unphysical results, such as 2500 K for the Co(1)Bi(1) sample, and even higher

for the Co(2)Bi(1). The bulk Curie temperature for Cobalt is well known to be at about 1388 K [57]. This fact suggests that the n exponent should be higher than 3/2. Additionally, by fitting with $n = 3$ more reasonable results are found, nonetheless. For a correct determination of *n* and T_curie the saturation magnetization should be measured at higher temperatures, above RT. (ii) One interesting trend in the fitting with $n = 3$ is a sequential reduction of the T_{Curie} with the Co thickness. It has been reported a T_{Curie} dependence on the thickness of ultra-thin films of cobalt [79]. These findings indicated that the reduction of cbalt thickness is followed by a decrease in the T_{curie}, which seems to be independent of the amount of bismuth. The reduction of T_{Curie} could be related to a finite size effect. When the thickness become smaller than the spin-spin interaction length [80], the overall exchange coupling is reduced.

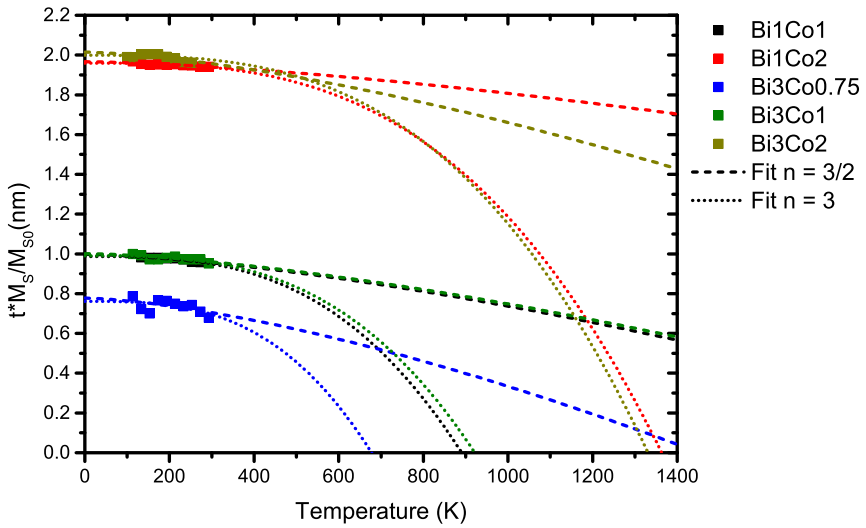

Figure 4.2 – Normalized Magnetization separated by thickness as a function of temperature for different samples

$$\frac{M_{sat}(T)}{M_{sat}(0)} = 1 - (\frac{T}{T_{curie}})^n \tag{4.1}$$

The ratio between the remanent magnetization and the saturation magnetization, known as squareness, was determined and is shown in the Figure 4.3, as a function of the temperature. Similarly to the saturation magnetization, the remanent magnetization of the samples have no dependence on temperature (in the measured range). In the graph, Co(2)Bi(3) and Co(1)Bi(3) are almost equals, but a rather small value of M_{rem}/M_{sat} for the sample Co(0.75)Bi(3) is seen. The decrease of the remanent (in plane) magnetization of samples with very small thicknesses could be related to changes in the magnetic anisotropy of the sample, such as the surface anisotropy

contribution to an out-plane magnetization component. However, no evidence of this kind of anisotropy was found in the Hall experiments (will be discussed further).

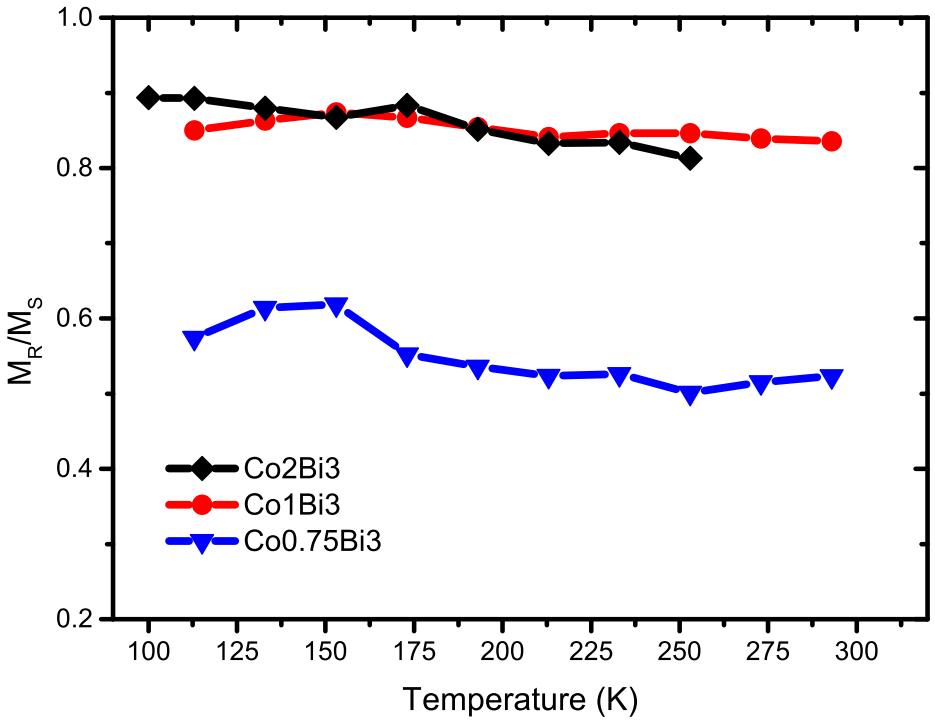

Figure 4.3 – Ratio between the remanent magnetization and the saturation magnetization as a function of temperature for samples with 3 nm of Bismuth.

4.1.2 Coercive Field

In the Figure 3.7 are presented the $M \times H$ measurements for the samples studied in this work. In the Figure 4.4, specifically, are displayed the hysteresis curve for the samples with Co(2) layers and different Bismuth layer thicknesses. These data were measured at room temperature (RT) by applying a magnetic field parallel to the samples' surface. It can be seen that the stacking with bismuth systematically turn the Co layers magnetically harder. As the Bi thickness is increased, the area enclosed by the hysteresis become larger. The blue dots represent the pure Cobalt samples, while the green dots are for the samples Co(2)Bi(3). Notice that the addition of Bi increases the coercivity from 80 Oe to about 240 Oe, a three-fold increment.

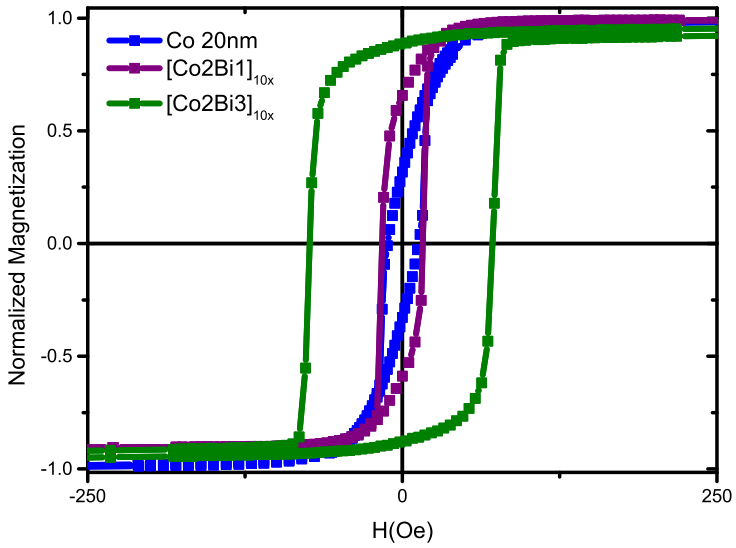

Figure 4.4 – Coercive Field data for different cobalt thicknesses in the presence of Bismuth.

Figure 4.5 summarizes the coercive field data of all studied samples, for distinct Co and Bi thicknesses. For pure Cobalt (reference samples), the coercive field barely changes by reducing the thickness down to 2.5 nm. By introducing 1 nm of Bi intercalated with the Co layers, a very distinct behavior is seen and the coercive field increases strongly with only with the reduction of the Co thickness. By further increasing the Bi thickness to 3 nm, the coercive field increase 4-fold and quickly rises by reducing the Co thickness. The increase of the coercivity is unexpected and usually the opposite is observed in the literature [81]. We speculate that the rise in coercivity is related to the DM interaction [82]. The DM interaction is known to dump the motion of the magnetic domains [29], which may increase the coercivity of symmetrical layers. Another effect of DM interaction is the horizontal shift of the hysteresis curve. However, this effect is only observed in asymmetrical stacked heterostructures [83]. Here, no shift of the hysteresis loop was observed.

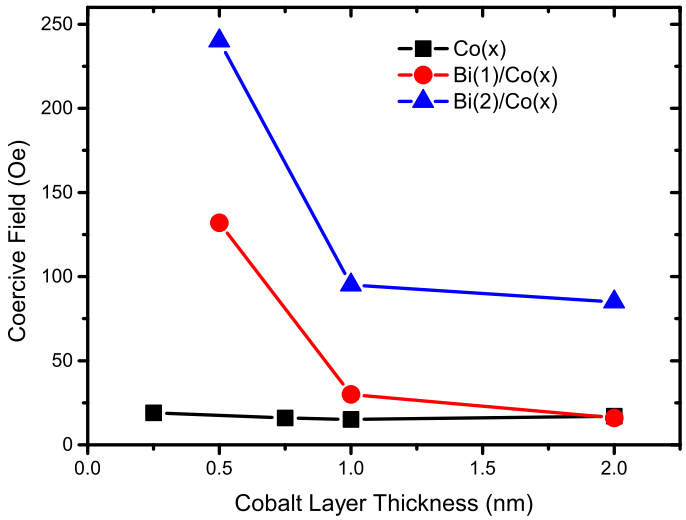

Figure 4.5 – Coercive Field data varying the Cobalt thickness in the presence of Bismuth.

An interesting comparison is the reference Cobalt sample with 2.5 nm thick. The coercive field is four times smaller than in the sample Co(2)Bi(3), which has 10 layers of Cobalt with 2 nm thick each. We expect that the microstructure of the 2 nm layer into the multilayer to be almost the same as in the reference sample with about 2.5 nm thick. So, the large increase in coercivity by intercalation of Bismuth layer cannot be explained just by microstructure arguments. Being reasonable to infer the rule of DM interaction. The DM interaction is a direct consequence of the strong spin-orbit coupling of bismuth layers.

The temperature dependence of the coercive field is displayed in Figure 4.6a. Notice that the coercive fields versus temperature were measured in magnetotransport experiments, since the $Mvs.H$ curves were measured only at room temperature. This graph shows that the reference Cobalt (20nm) sample has a distinct behavior in comparison to the Co(2)Bi(3) and Co(1)Bi(3) heterostructures, which present an almost linear increase of coercivity by lowering the temperature.

The correspondence between the hysteresis curve and the magnetotransport curves is shown in Figure 4.6b. At the same position where the magnetization reversal occurs, a magnetoresistance peak is observed. The increase of the coercive field by lowering the temperature is rather expected, once at low temperature the magnetic domains start to froze at low temperatures. The power law decrease of the coercive field upon rising the temperature can be empirically described by the Kneller's Law [84, 85], given by the Equation 4.2, where the $H_c(0)$ is the coercive field at zero temperature and the T_B is the blocking temperature where the magnetic moments start to

freezing. For the reference sample Co(20nm) at low temperatures, the α exponent fits well the expected $\alpha = 0,5$ value, usually attributed to non-interacting magnetic domains with low size dispersion [84]. At high temperatures the H_c is almost constant. For the samples Co(2)Bi(3) and Co(1)Bi(3) the α parameter is 1. This behavior may be related to the ordered layers stacking of these samples. For the sample Co(0.75)Bi(3) the α is again 0.5, possible indication that small Cobalt particles are being formed in this sample.

$$H_c(T) = H_c(0)[1 - (\frac{T}{T_B})^{\alpha}] \tag{4.2}$$

(a) (b)

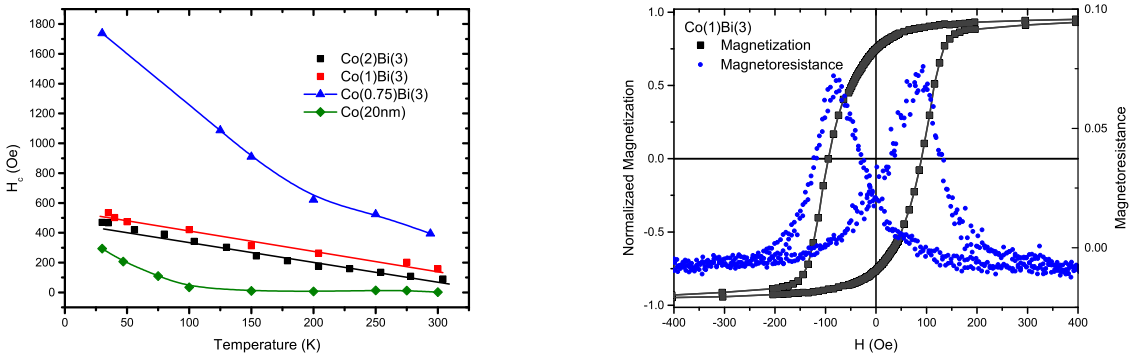

Figure 4.6 – (a) Coercive Field data vas a function of the temperature for different samples. (b) MRT and the magnetization as a function of the magnetic field applied to the sample.

4.2 Transport Results

4.2.1 Electrical Resistivity

In Figure 4.7 is presented the dependence of the electrical resistivity against temperature, from 2 K to 300 K. All the data were normalized by the respective RT resistivity. Such a normalization was done to fit all the data in the same scale. Figure 4.8 shows the absolute values of the electrical resisitivity vs. temperature data are presented. In the Figure 4.7, one can see that there is a crossover from a negative temperature coefficient (NTC), i.e., a decrease of the resistivity for increasing temperatures (as verified for the bismuth data) to a positive temperature coefficient (PTC), in the cobalt data, by increasing the Cobalt content in relation to bismuth. We analyze the results on the base of a two-resistor association, one from bismuth layers and another from cobalt layers. Although the best results was found by using a serial configuration, we notice

that due very low thicknesses of the layers, the system should be described by a rather complex resistor series-parallel association to fully described the data. Now we proceed with a qualitative description of electrical properties of the samples.

The Cobalt resistivity vs. temperature curve shows a linear increase of resistivity at high temperatures, but below 40 K it saturates to a value known as residual resistivity. The residual resistivity ratio (RRR) - the ratio of RT resistivity by the residual resistivity - for the reference sample of cobalt (20 nm) is about 1.25. Values between 1.2 and 2.0 are commonly reported for cobalt thin films [86, 32], depending mostly on the film thickness. For bulk and single crystal samples, RRR value as high as 380 can be found [87]. The reason for the low RRR in thin films is the scattering at the surfaces and grain boundaries. Although the RRR of cobalt samples can be found in a large range of values, the overall behavior of the curves is always the same, typical from transition metals [47, 57]. High RRR implies in high phonon scattering of carriers and low amount of cristalline defects.

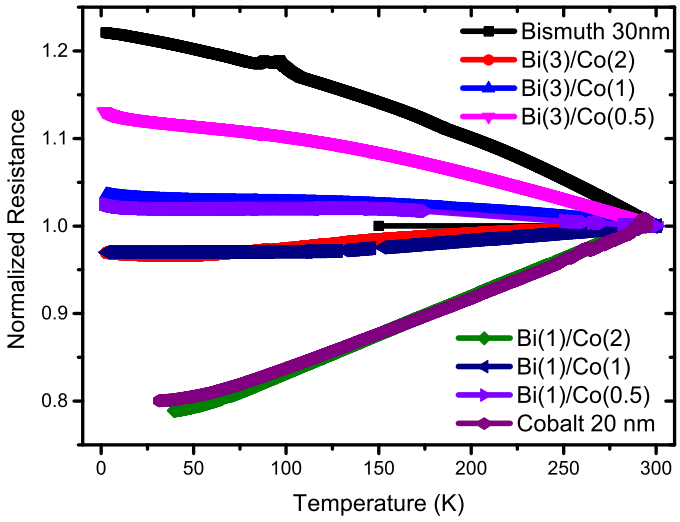

Figure 4.7 – Resistance normalized by the room temperature resistance as a function of temperature for different multilayer samples.

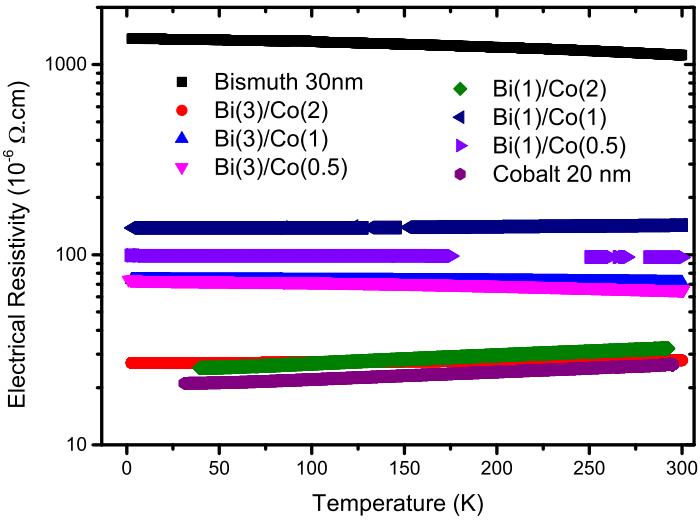

Figure 4.8 – Comparison of different behavior of Resistance for the samples.

In the case of the bismuth thin films, the resistivity behavior is highly dependent on the samples preparation conditions for the sample preparation, such as crystallinity, defects and thickness. For instance, single crystal usually presents PTC [88], while, thin films presents NTC [89, 90], due to effects of grain boundaries. Still, in low thickness samples, the role of surface conduction may also be relevant, changing the behavior of the thin films to PTC [90]. So, it is impossible to simulate the resistance of the heterostructures by simply using the resisitivities of stand alone reference samples, such as Co(20nm) or Bi(30nm). The high value of electrical resistivity found for the samples with high amount of Bismuth, or even as in the case of the Bi30 sample, indicate that the bismuth layers in the heterostructure is rather semi-metallic (ruled by grain boundary scattering) than metallic (as expected for samples of very low thickness [90]).

The resistivity of Co(2)Bi(3) sample shows an increase of resistance when the temperature, while in the Co(1)/Bi(3) sample the resistivity decreases. Figure 4.9 shows the Resisitivity versus Temperature measurements of samples with Bi(3) layers. In the Figure 4.9a, an interesting characteristic occurs below 40 K, displaying a minimum followed by an inverse R vs. T behavior at the lowest temperatures. The same result was observed in two identical samples. Such an increase of resistivity at low temperatures could not be explained as simple combination of Bi and Co serial or parallel resistors. Notice that below 40 K the Co resistivity begins to saturate at the residual value, so the increment in the heterostructure might come from Bi layers. However, the R vs. T curve of Bi reference sample displays a negative curvature (concave), as in Figure 4.9d, while the curvature of sample Co(2)Bi(3) showed a positive curvature (convex). The same

effect is seen in the samples Co(1)Bi(3) and Co(0.5)Bi(3), in Figures 4.9b and 4.9c, respectively. Such results can be interpreted as two different phenomena: (i) some oxidation of thin Bismuth or Cobalt layers that introduces in the system a semiconductor like behavior, operating as a third resistor component. Nevertheless, both Cobalt oxides and Bismuth oxides are highly insulating, with bandgaps larger than 3 eV, this hypothetical oxidation is rather unlikely to contribute to the overall resistivity of the Heterostrucute. (ii) The possibility of a Kondo-like effect, in which the Co impurities diffuse into the Bi layers acting as local magnetic moments and interacting with the free electrons of bismuth. Notice that this later possibility is also unexpected, since bismuth has a vanishing free electron density. However, some results have being reported in literature proposing the possibility of Kondo Effect in systems such as Bismuth doped with magnetic impurities [91, 92, 93].

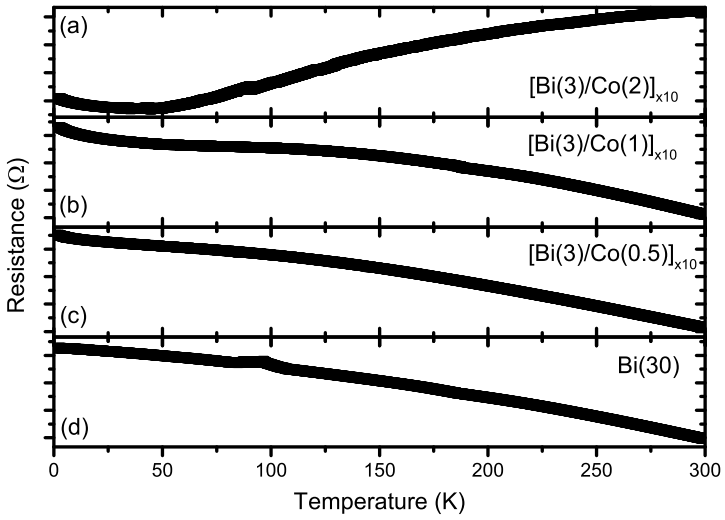

Figure 4.9 – Comparison of different behavior of Resistance for the samples.

4.2.2 Magnetoresistance

The magnetoresistance of the studied samples were measured in both, longitudinal and transverse configuration. Measurements were carried out in between 30 K and RT, with applied magnetic field up to 2 kOe. Figure 4.10 displays the data obtained from the sample Co(2)Bi(3) in both field configurations and at 30 K. The longitudinal magnetoresistance, the MRL, is presented in black dots. The measurement starts at -2 kOe, the magnetization of the cobalt layers is saturated and aligns with the applied field, which is parallel to the electrical current. By reducing the field, at the coercive field, the magnetization rotate 180 ° to reverse the magnetization. In this process,

the magnetization becomes perpendicular to the current, as depicted in the Figure 4.10. In this situation the resistivity reduces, which is related to the suppression of scattering of s electrons by the Co magnetic moments. Such scattering process is a spin-orbit driven phenomena. In red dots, is the transverse magnetoresistance (MRT). The curve starts in -2 KOe with the magnetization and current perpendicular to each other, given a reduced resistivity. At the coercive field the magnetization rotate and the current and magnetization become parallel increasing the resistivity. The behavior shown in the Figure 4.10 is known as the anisotropic magnetoresistance (AMR) of a ferromagnetic metal. This effect was firstly described by Fert and Campbell [59] and after by Kokado, et al. [60]. For more information about the AMR we refer to the proper section at the chapter 2. Here, the key information is that the AMR amplitude, i.e., the difference between the MRL and MRT configuration is proportional to the spin-orbit coupling of the carriers.

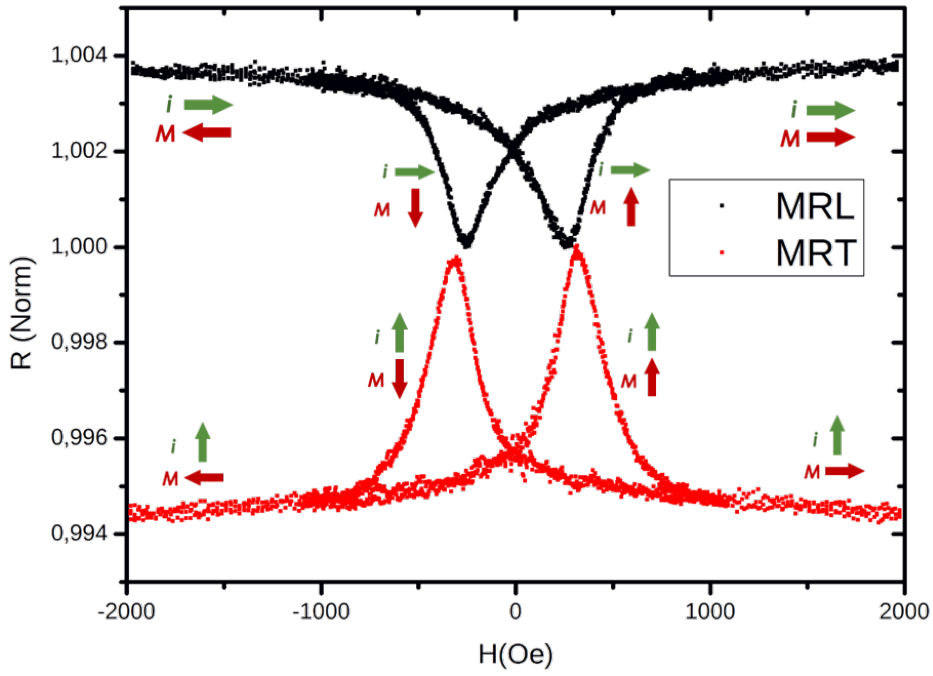

Figure 4.10 – Normalized MRL and MRT data for Co(1)Bi(3) at T=30k

As a general trend in the AMR measurements, we point out that there are small differences in the MRL and MRT, such as: (i) distinct coercivities, as can be seen in Figure 4.10, and (ii) the distinct intensities in MRL and MRT (usually for bulk systems, the MRT is larger than MRL). Both effects signaled above are directly related to the in-plane anisotropy of the samples, which in turn, is dependent on the samples' preparation conditions.

Figure 4.11 presents the MRL of the sample Co(2)Bi(3), measured at different temperatures. Two characteristics can be pointed out, a very small change in the MRL intensity, i.e., the magnetoresistance ratio, given by the Eq. 1.13 barely changes with the temperature. The decrease of the temperature increases the coercive field, as discussed before. We analyze the intensity of the AMR by using the MRL data in order to evaluate the spin-orbit coupling in the samples with different thicknesses of Cobalt and Bismuth.

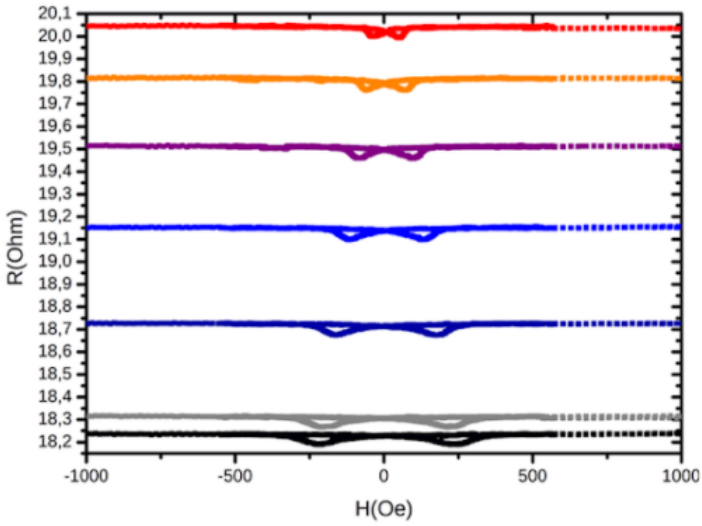

Figure 4.11 – Longitudinal magnetoresistance for Co(2)Bi(3) at different temperatures

In the Figure 4.12 is shown the percentual MRL intensity, as a function of the temperature for the samples containing Bi(3) layers. It was not possible to measure a reference samples containing only 2 nm Cobalt. The results for the samples Co(0.75)Bi(3) and Co(2)Bi(3) indicate that the MRL ratio are smaller than the samples Co(1)Bi(3) in all measured temperatures. Additionally, the temperature profile of the samples Co(1)Bi(3) is different from the other two samples, which are constant upon the temperature variation. The Co 20nm MRL ratio is also independent from temperature. For the case of sample Co(1)Bi(3) the MRL ratio increases as temperature is lowered.

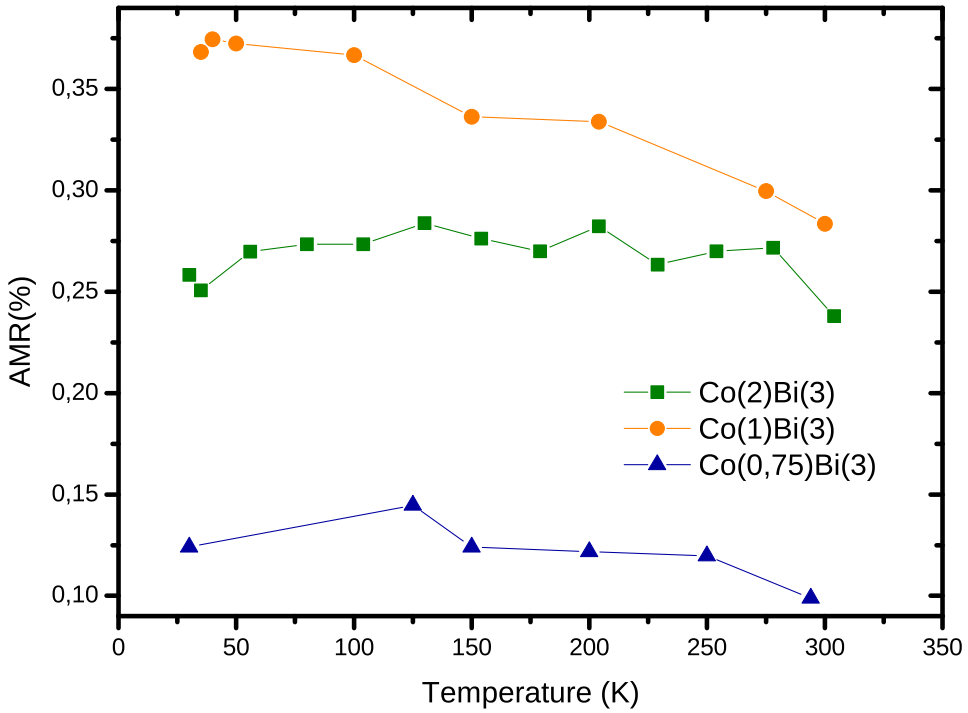

Figure 4.12 – Anisotropic magnetoresistance (AMR) as a function of temperatures for different samples

The MRL ratio as a function of Cobalt thickness, for the samples with Bi(3) layers is displayed in the Figure 4.13 for low and room temperatures. We expect a monotonous augmentation of the AMR ratio by increasing the Co thickness, until a saturation is reached at thick Co layers. At very low Co thicknesses, the current mostly flow through the Bismuth layers, which do not display the AMR ratio. By increasing the Co content, the current at the Bismuth layers is much smaller and the overall AMR ratio is the one for bulk Cobalt. However, this was not observed. Notice that the highest AMR ratio was found for the Co(1)Bi(3), followed by a decrease for thick Co layers (as Co(2)Bi(3)). The temperature dependence is negligible. It is possible to relate the AMR peak to the spin-orbit interaction, as it tends to mix channels with opposite spins [60].

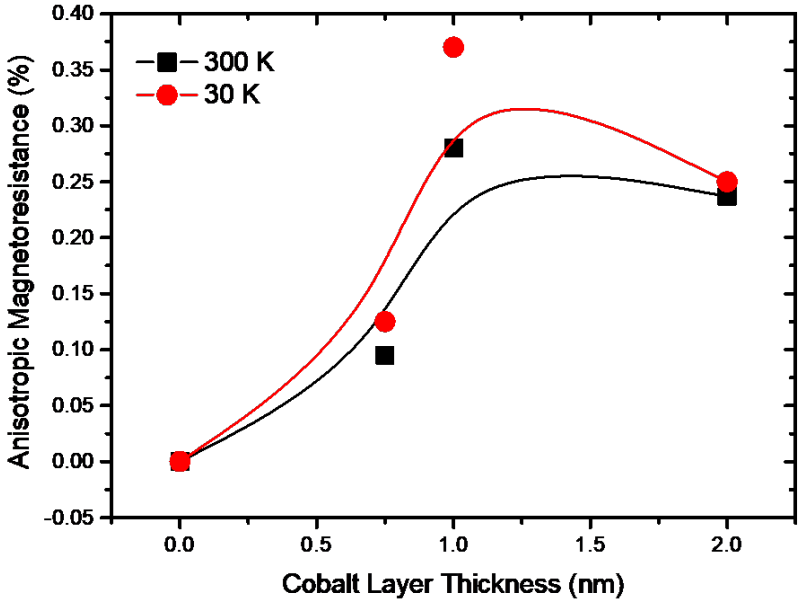

Figure 4.13 – Anisotropic magnetoresistance (AMR) as a function of Cobalt thickness for 35K and 300K

These results strongly suggest a relation between the thickness of Cobalt and the SOC effect, as the peak observed in the AMR data does not follow the expected behavior with the increase of Co layer thickness in the multilayer system.

4.2.3 Hall Effect

The measurement of the Hall effect in the heterostructure Co(0.75)Bi(3) and Co(2)Bi(3) are depicted in Figures 4.14a and 4.14b, respectively. The S-like shape of the curve is characteristic from the Anomalous Hall Effect, here, due to the Cobalt layers. The fast increase in Hall resistivity at low magnetic fields is the AHE, in which the magnetization abruptly changes the transport properties. The linear behavior at high magnetic fields is the ordinary Hall effect due to cyclotron motion of carriers. By using the procedure described in the chapter 2 we obtained the anomalous Hall coefficient (R_s).

(a) (b)

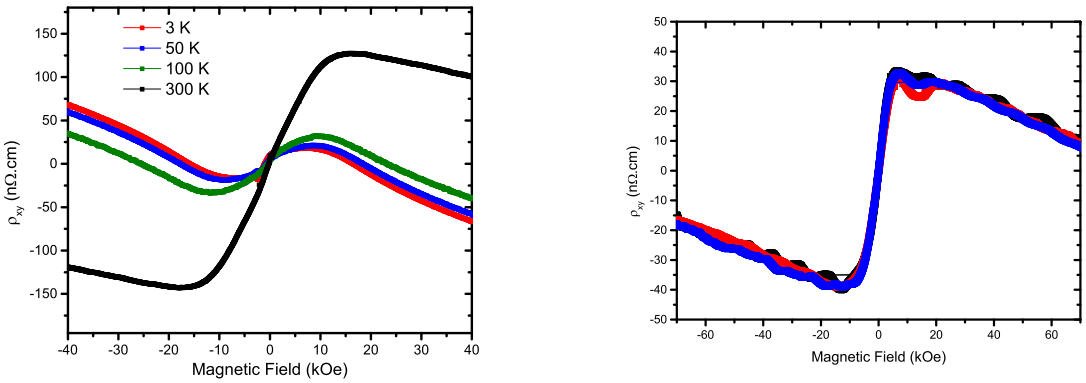

Figure 4.14 – In (a)Hall Effect measurements for the sample Co(.75)Bi(3) for different temperatures. (b) Hall Effect measurements for the sample Co(2)Bi(3) for different temperatures. In Black for 3K, red for 10 K and blue for 20 K.

Figure 4.15 shows the anomalous Hall Resistivity (AHR) for the samples with Bi(3) and Bi(1) layers vs. Co thickness, at three distinct temperatures. Notice the same profile as the Magnetoresistance results, i.e., a maximum value of Hall resistivity for samples with about 1 nm of Cobalt Layers. Nevertheless, in contrast to the MR results, some other features can be observed: (i) The Hall resistivity is highly temperature dependent. Higher is the temperature, larger will be the Hall resistivity will get higher as well. (ii) Looking to the eye guide lines in the graph, one observes that the increase of the temperature seems to push the peak to small values of Co thickness. The filled symbols are data for the samples with 3 nm Bismuth layers, while the open symbols hold for samples with a layers of 1 nm of Bi. Samples with 1 nm Bi layers do not showed the peak in the Hall resistivity. The stars in the Figure 4.15 are values for Hall resistivity obtained from the literature [94], for a single layer of cobalt. Notice that the values found in literature are smaller than those found here, for the Co/Bi heterostructures. The anomalous Hall resistivity is directly related to the spin-orbit coupling of the carriers, so the increase in the Hall resistivity could be taken as an evidence of enhancement of the spin-orbit coupling.

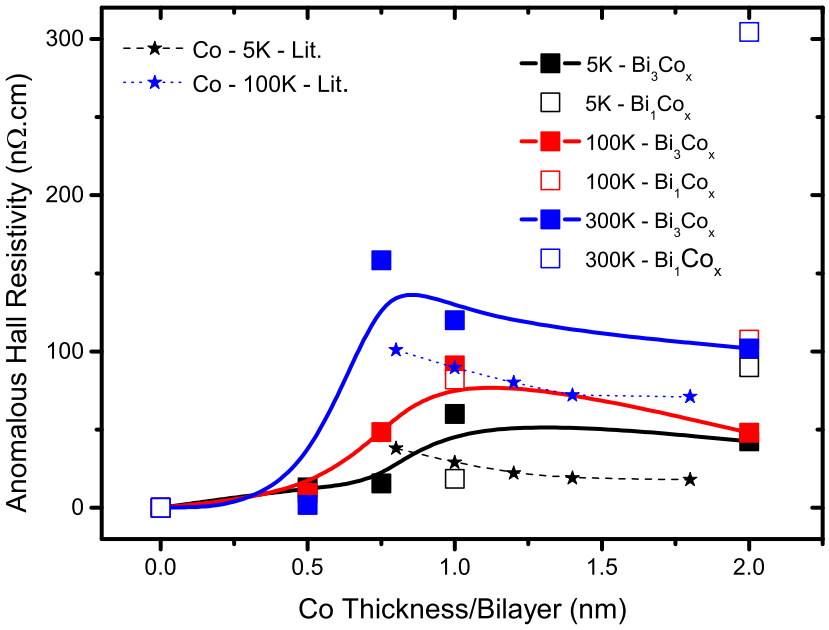

Figure 4.15 – Anomalous Hall resistivity measurements as functions of Cobalt thickness in 5K, 50K and 100K

In the Figure 4.16 is plotted the AHR vs. Temperature for the samples with Bi(3) layers. The raise of temperature should increase the AHR. However, that is not the case for the sample Co(0.5)Bi(3) which shows a reduction of AHR by raising the temperature. This inverse behavior is not well understood, and we speculate that it is related to the ultrathin Co thickness. In the Figure 4.17 is presented the graph of AHR vs. Resistivity (ρ_{xx}). Here, we point out that was not possible to separate the Cobalt contribution from the overall heterostrucutre resistivity. Then, for this analysis we have used only the reduced resistivity of the reference Co(20nm) sample. Notice that for all samples (except for Co(0.5)Bi(3), which has a non usual behavior) the AHR scales linearly with the ρ_{xx}. This indicates that the origin o AHE come from extrinsic scatter mechanism known as skew scattering, described in Section 1.4.4. In this mechanism, the spin-orbit of a impurity, here the Bismuth at the interface, scatter the electrons generating the AHE. This is in opposition to what is expected for bulk Cobalt, in which a intrinsic mechanism is the responsible for the AHE [94, 95].

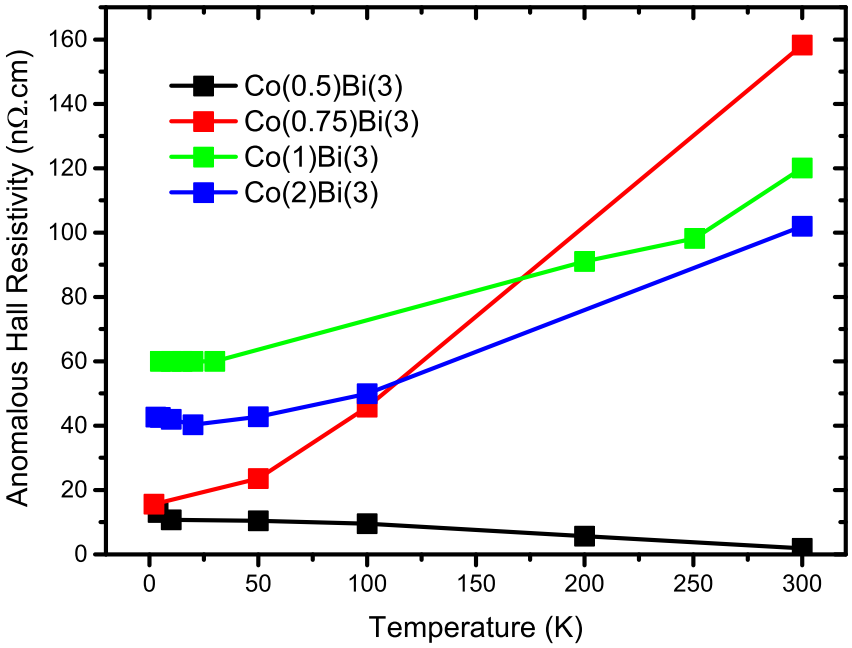

Figure 4.16 – Anomalous Hall resistivity measurements as a function of temperature

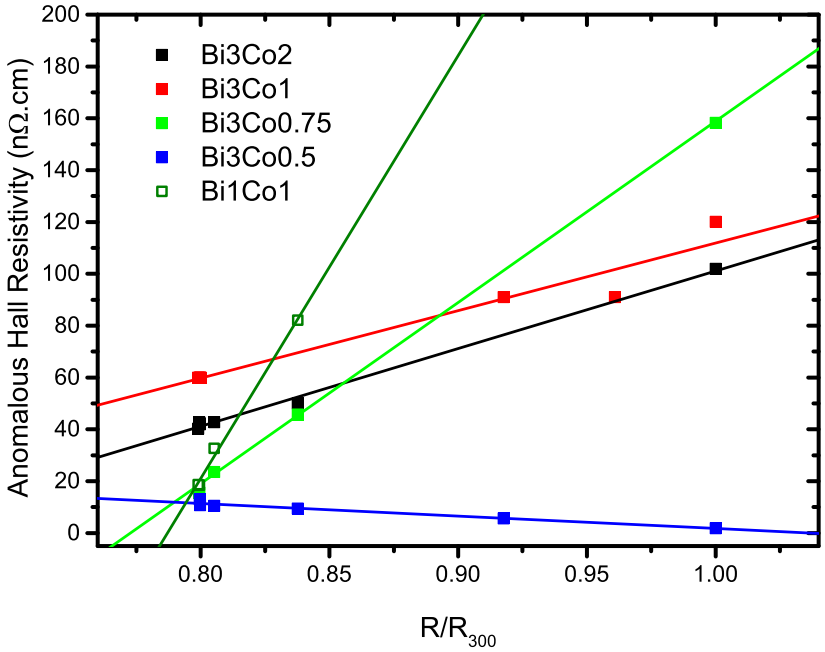

Figure 4.17 – Anomalous Hall resistivity measurements as a function of normalized resistivity

5 Discussion

In this work, we focused in understand the proximity effect of high spin-orbit layer and ferromagnetic layers stacking in multilayers heterostructures by using Bismuth as spin-orbit material (SOM) and Cobalt as Ferromagnetic material. We mainly look for spin-orbit effects induced in the Cobalt ferromagnetic layers due to the proximity with the Bismuth layers. Here, we are going to address some point in order to focus on the results. Our findings seems to support a kind of spin-orbit proximity effect driven by the scattering of carriers at the interfaces by impurities with very strong spin-orbit coupling. The discussion is presented below.

We start discussing the coercive field of the heterostructures, presented in the section 4.1.2. Here, our results point to a increase of coercive field by increasing the Bismuth thickness in the multilayers. We attributed this enhancement to the presence of an additional exchange interaction at the interfaces known as Dzyaloshinskii–Moriya interaction (DMI), which is a antisymmetric type of exchange interaction. The symmetric disposal of layers possibly kill any ordering that may be induced by the DMI. Still, the DMI can dump the domain wall motion, which may, in turn, increase the coercivity. Similar results for the increase of Coercivity by mixing Bi and Co were found by Honda et al. [3]. Notice however, that such effect is not due to any proximity effect, and occurs only at the interface.

Two other very interesting results are the AMR and AHE, for the different samples produced in this work. The results are summarized in the Figures 4.13 4.15. Both results, from independent phenomena, points to and increase of the spin-orbit coupling up to 1 nm of Co, followed by a decrease for higher thicknesses. For the case of AMR, similar results have been shown by Honda et al. [3], for Bi/Co mixture. The increase of AMR ratio at very low thickness have being attributed to two different trends: (i) The presence of a shunt due to the overall multilayer structure, i.e., at very low Cobalt thicknesses, the current flow thru the Bismuth only, and no AMR ratio is seen [96] (ii) The possibility of a dead magnetic Co layer at the interfaces in very low thicknesses [97], our magnetization data for low thicknesses samples shows no dead layer, nonetheless. In addition, the decrease of AMR ratio above 1 nm Co thickness is not expected. Tokaç, et al. [97], found a saturation of AMR ration at high thickness at the bulk value, for Cu/Co multilayer. Same saturation was found for NiFe [98]. Here, we suppose the existence of SOC proximity effect (SOPE) which exist near to the interfaces, which enhance the AMR

ratio. Our hypothesis is resumed in the Figure 5.1, in a schematic of the distinct contributions to the AMR. Notice that such SOPE could be a effect of interface scattering so the range where it take place should be around the bulk scattering length (carrier mean-free-path) from interface, that for the Cobalt is about 7 nm [97].

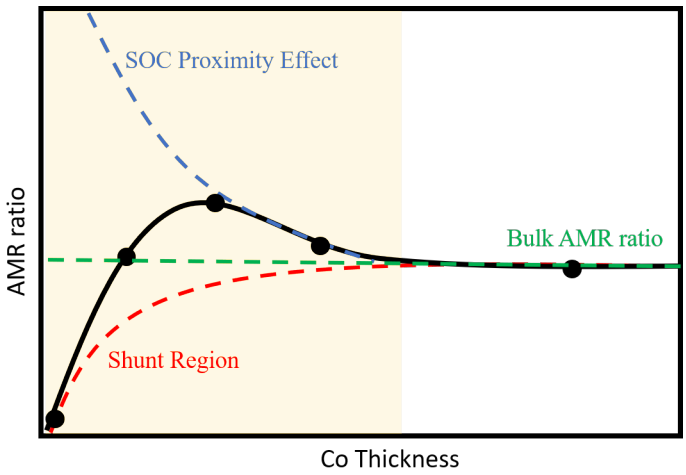

Figure 5.1 – Schematic of the AMR measured in the samples with the effects which occur by raising the Co thickness.

In the data for AHE the same behavior is seen, i.e., the increase of SOC at low thicknesses. Similar results were published by Zhang, et al [2], showing a peak behavior of AHR at CoFeAl(CFA)/Platinum interfaces. They argue that a SOC proximity effect is responsible by the phenomenon. Notice that Zhang, et al, also shown that FM interfaces with low spin orbit material do not show the peak profile, and there is also a 10-fold increase of AHR due to proximity effect. Our data shows the fast increase of AHR at low thicknesses that, as well as the AMR data, could be related to the shunt of the Bismuth layers. The decrease of AHE above 1 nm thick Cobalt Layers is related to the SOPE. Here the increase of AHR was calculated in relation to the AHR of the samples with higher thickness, it means an increment of about 1.5x. Using the same methodology for the data of Zhang et al. it means an increment of about 3x. Such difference could be related to orbital effects, once in CFA/Pt interfaces, the SOC is mainly due to d-orbital, while in Co/Bi, the SOC is related to p-orbitals. We also compare our data with AHR of pure Co thin films, found in the reference [94], these data is presented in star symbols in the Figure 4.15. Notice a systematic increase of 1.5x in AHR, in relation to the Co thin films, in all thicknesses compared, which is an additional evidence of SOPE. The increment of AHR by interfacing with high spin-orbit materials was also observed by Zhang, et al [99], which also shown that the multilayer stacking reduce the AHR value in relation to bilayers.

Another important result of our work is the comparison of AHE mechanisms, here, we show that the Anomalous Hall Coefficient follows a linear relation with the longitudinal electrical resistivity. This is further related with the extrinsic Skew Scattering mechanism. For pure Cobalt thin films, the intrinsic mechanism is expected [94, 95]. These AHE results support our AMR results which also point for a SOPE due to elastic scattering with high spin-orbit impurities at the interfaces. Changing the scatter mechanism from intrinsic to extrinsic. A scheme of the SOPE induce by skew-scattering at the interface is given in the Figure 5.2.

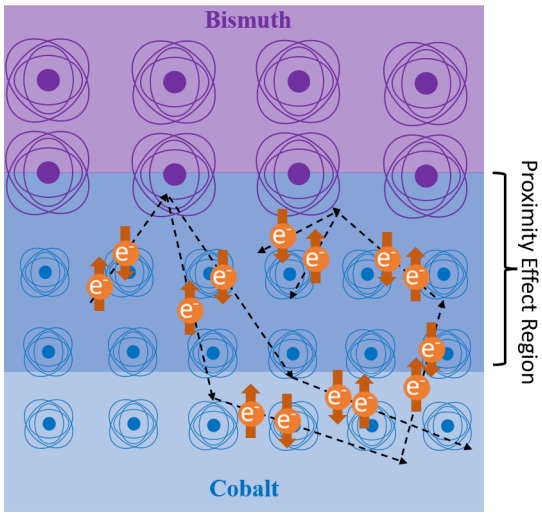

Figure 5.2 – Illustration of Spin-Orbit Proximity Effect based in the scattering of carriers at the interface.

In order to further understand the proximity effects of SOC in the samples, we employed Density Functional Theory (DFT) ab initio simulation. The DFT simulation was done as a collaboration with advisor in this work, Professor Milton Andre Tumelero. The DFT full results and discussions are presented in the Appendix A. The DFT results could be summarized in four main findings, that are: (i) There is an increment in the Density of States of Bismuth close to the surfaces/interfaces, in comparison to the bulk, which should enhance the electrical conductivity and increase the electron-electron scattering. (ii) There is some changes in Cobalt electron distribution when interfaced with Bismuth in comparison to the Cobalt electron distribution at surfaces. The electrostatic potential barely changes in the cobalt side of the interface, nonetheless. The electrostatic potential over Bismuth layers changes in the first layer close to the interface. (iii) A very interesting finding is the rise of magnetic moments in Bismuth layers close to Cobalt interfaces that could be related to another type of proximity effect, the Magnetic Proximity Effect.

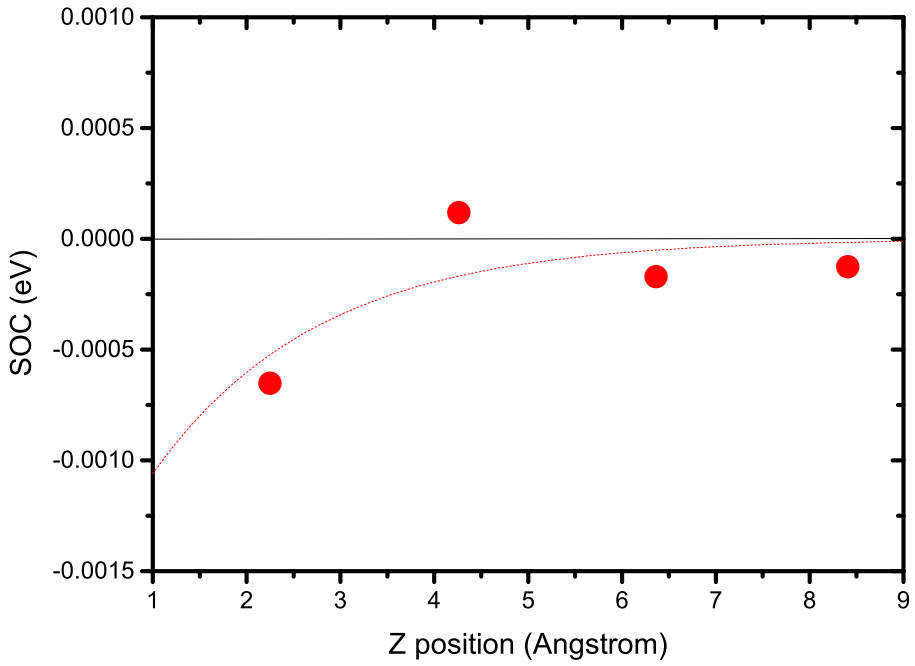

Figure 5.3 – SOE for cobalt atoms as a function of the z position starting from interface. Four Cobalt layers were used in the simulation.

The last interesting finding, the (iv), is the increase of Spin-Orbit Energy (SOE) in Cobalt layers close to the interface with Bismuth. The Figure 5.3, is presented the graph of SOE around a Co/Bi interface simulated with DFT. The data is the SOE of Cobalt layers. The zero in the x-axys is the interface and at about 8.5 A, is the surface of Cobalt. This graph is a Zoom of the Figure A.7. Such increase in the SOE is related to the polarization of electrons orbital at the interface, which get distorted due to Bi atoms. It is important to notice that the increase in the SOE is quite local, only in the first Co layer at the interface. Such SOPE is due to orbital hybridization. The increase of 0.00075 eV in the SOE at the interface is about 5 per cent of enhancement in relation to the Bulk SOE. Such increase in the SOE due to hybridization is probably the same type of SOPE seen in Graphene [41, 42]. We point out that the SOPE effect seen in this work is much longer range than the one predicted by DFT simulations.

6 Conclusion and Perspectives

In this work, two different methods for measuring the spin-orbit coupling using electrical techniques were used. We measure the Anisotropic Magnetoresistance and the Anomalous Hall Effect of the samples. Both effects point to an increase of the SOC at the interface of the multilayer in thicknesses of up to 1nm, which can be considerate a long range effect.

We also test different thicknesses of Cobalt and Bismuth in the multilayer systems, which point out to an optimal proportion of Co and Bi to achieve higher influence of SOC at the interfaces. Other works in this area have also found the same type of behavior of AHE in magnetic multilayer systems [2], here, the result are confirmed by other different measurements. The outcome obtained from studying these multilayers systems will guide and assist the development of new structures which are looking for enhance SOC in magnetic systems.

Comparison of AHE mechanisms shows that the Anomalous Hall Coefficient follows a linear relation with the longitudinal electrical resistivity. This is further related with the extrinsic Skew Scattering mechanism. For pure Cobalt thin films, the intrinsic mechanism is expected.

APPENDIX A – Computational Results: DFT (Density Functional Theory)

In order to further understand the Bi/Co interfaces looking for the magnetic and spin-orbit effects, atomistic simulations were performed by means of Density Functional Theory [100]. The simulations were not the focus of this work and were done to support the experimental findings and interpretation. The simulations were done the advisor and his collaborators using the VASP (Vienna Ab initio Simulation Package) [101] running at the CENAPAD/SP computation canter at Campinas University (UNICAMP). The mains findings from DFT results are presented in chapter 5 - Discussions and some support results as well as the calculation parameters are presented below.

A.1 Simulations Parameters and Methods

The VASP code is based in periodic boundary conditions and optimized for 3D crystal structures. The package solve the Kohn-Sham [102] equation in a self-consistent fashion. The electron orbital are spanned in a plane wave basis set allowing fast and easy code implementation.The calculations are based in pseudopotential method, where the atomic exact electrostatic potentials are substituted by an artificial one which essentially separate the potential in two parts, one that represents the valence electrons similarly to the exact potential, and another part which is mathematically treated by the Projector Augmented Waves (PAW) [103] Method. This methods help to overcome the computational problems (high amount of plane waves) in describing the rapid oscillations of orbitals from electrons close to the nucleus. In simple, the PAW method introduce pseudo-orbital wave functions which outside of sphere centered at the ion nucleus lead to same eigenvalues spectrum as the exact potential. Inside of this sphere, the contribution from pseudo-orbital can be removed and substituted by the exact orbital from atomic potentials. Inside of the sphere the orbitals are not spanned in plane waves basis set but with a spherical harmonics basis set. The pseudotential used for describe the Cobalt atoms have the follow valence electrons Co:[Ar]3d8 4s1, while for bismuth atoms the follow pseudopotential was used Bi:[Xe]7s2 6d10 6p3.

The approximation picture of the simulations comes from the chose of the correlation-exchange functional (XC). Here we used the PBE [104] functional (Perdew-Burke-Ernzerhof). This functional is one of the non-local functional based in the GGA approximation [105] (Generalized Gradient Approximation), which improve the XC description based on Local Density Approximation [106] (LDA). The PBE gives a very good description of the electronic and structural properties of metallic solids [107].

The calculations parameters and convergence criteria used in this work are: (i) orbital plane wave energy cutoff was 320 eV. (ii) The convergence threshold for the auto-consistent cycle was 1E-6 for electronic calculation and 1E-8 for spin-orbit energy calculations. (iii) The k-mesh for fast Fourier transform for all the structures simulated were 12 x 12 x 1, give a total of irreducible K-points (points in the reciprocal space) of 144. (iv) For the structural relaxation the, the convergence criteria was the sum of all force have smaller value than 0.01 eV/A.

A.2 Atomic Structure

For the simulation of 2D atomic cell the supercell method was applied. The cell was constructed by overlaying a cobalt hexagonal cell (R3M) with dimension 2x2x4 over a hexagonal bismuth cell (R3M) with dimension of 1x1x2. The obtained structure is a bi layer composed of 12 atoms thick of bismuth layer interfaced with 4 atoms thick cobalt layer. In order to trick the z-Axis periodic condition, we added above the cobalt layer and vacuum space of 2.5 nm. Such vacuum introduce a large distance which minimize the interaction (both hybridization and dipolar) of top cobalt atoms with the bottom bismuth atoms creating two surfaces instead a second interface. In order to fit the lattice parameters, the bismuth cell was strained to have an 4 percent higher lattice parameter, while the cobalt cell has negative stain of about 4 percent as well. The resultant cell is presented below in Figure A.1.

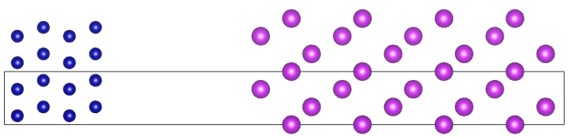

Figure A.1 – Supercell, Bi12Co4, used for the DFT calculations.

A.3 Density of States

Here we present the density of state (DOS) of the structures. In Figure A.2a, the DOS for the solid bulk bismuth and for a bismuth slab. The bismuth slab is created by removing the Co atoms from the supercell describe above. The bunch of states in between -5 eV and the Fermi Level are due to 6p orbitals. The states at about -10 eV are from 7s orbitals. The bulk spectra show the typical behavior expected for the bismuth, the suppression of the DOS close to the Fermi level, which characterizes the semimetallic behavior of bismuth, showing a very low carrier density. Such result of bulk simulation is a benchmark for all the calculations done here. For the slab DOS one can see that suppression of the DOS does no occur anymore. Such high density of state at Fermi level is due to dangling bond at the bismuth surface, and give to the bismuth surface a metallic behavior rather and semimetal. Such high value of DOS for the slab does no depend on the relaxation of the atoms at the surface. The metallic behavior of bismuth ultra thin layers have been experimentally observed before [90]. The Figure A.2b display the bulk cobalt DOS, the spin polarized DOS are as expected. This DOS is also a benchmark to support the calculations.

(a) (b)

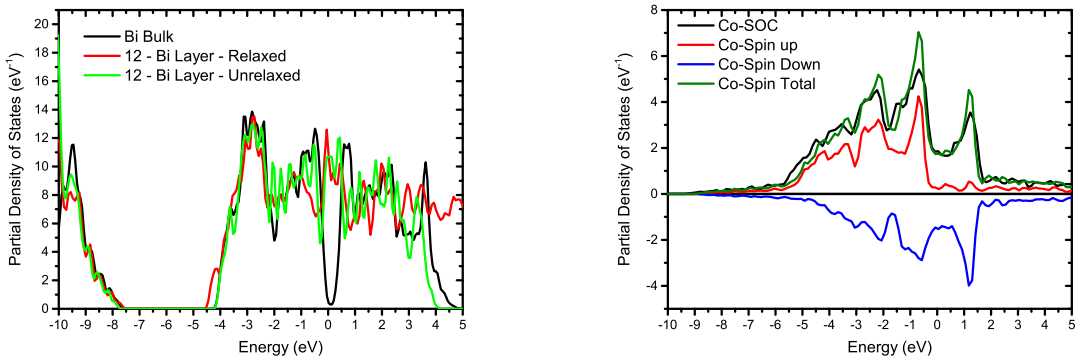

Figure A.2 – In (a) density of states for the bismuth slab and bulk solid bismuth. (b) Density of states of the bulk cobalt.

In the Figure A.3 is shown the DOS for the Bi12Co4 supercell. In the Figure the DOS of Bi12 and Co4 slabs are also presented. One can see that the there is a reduction of the Bismuth contribution to the DOS at Fermi level. It is related to the attenuation of the dangling bonds at the interface. No changes in the cobalt DOS could be found in the supercell in comparison to the cobalt slab.

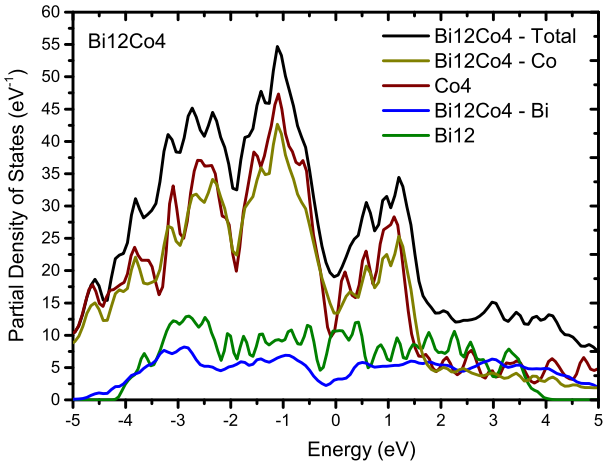

Figure A.3 – Partial density of states for the Bi12Co4 supercell and the comparison to the DoS of the individual Bi and Co slabs.

A.4 Charge and Spin Densities

The charge densities around the atoms of the supercell are presented in the Figure A.4a. The charges in the bismuth layers are highly localized in the xy planes of the hexagonal cell. The charge of the interface bismuth is distorted in relation to the inner bismuths, which is result from the hybridization to the cobalts at de interface. The Figure A.4b displays the spin asymmetry densities near to the interface. Notice the almost no spin magnetic moment is seen in the Bismuth atoms, while the spin distribution along the cobalt atoms at the interface are pretty different from the inner cobalt or even from the surface cobalt. The surface cobalt (to the right of the figure) shows an elongated structure resemble an egg, which is caused by the surface where the inversion symmetry of cobalt layer is broken, indicating a change in the magnetic moment of the surface Cobalt. At the interface, the spin structure shows the same elongated structure form some atoms, but a more symmetrical distribution for other atoms. There are two types of cobalt at the interface, as can be seen in the inset of Figure A.4b, three a close to the interface bismuth, while the fourth cobalt atom is far from the bismuth, and presents a spin distribution close to the cobalt from the surface.

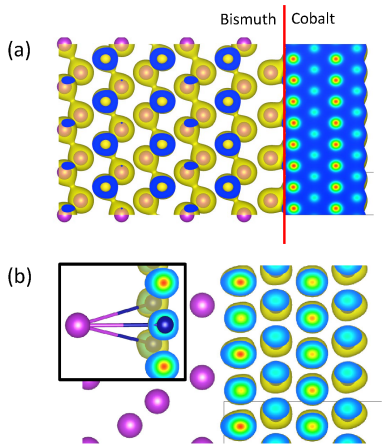

Figure A.4 – In (a) the charge density along the Bi12Co4 supercell. Isosurface 0.05. In (b) the spin distribution along the interface and in the inset, a zoom over the Bi-Co bondings, isosurface 0.0005.

A.5 Electrostatic Potential

Looking for electric field built in the interface we have calculated the electrostatic potential over the supercell. The results are shown in Figure A.5a. Notice that far from the interface the electrostatic potential from the supercell and the Bi and Co slabs are really similar, as expected. Close to the interface some trends could be better observed at the Figure A.5b. The electrostatic potential over the Co part of the interface fits well the potential from the Co slab indicating that there is no electric field over the cobalt atoms. On the bismuth part of the interface we can see that the potential from the bilayer changes in relation to the Bi slab, indicating that some electical field over the Bi atoms down to two layers of Bi. Such electrical field could be attributed to migration of electrons from Co to Bi site due to orbital hybridization.

(a) (b)

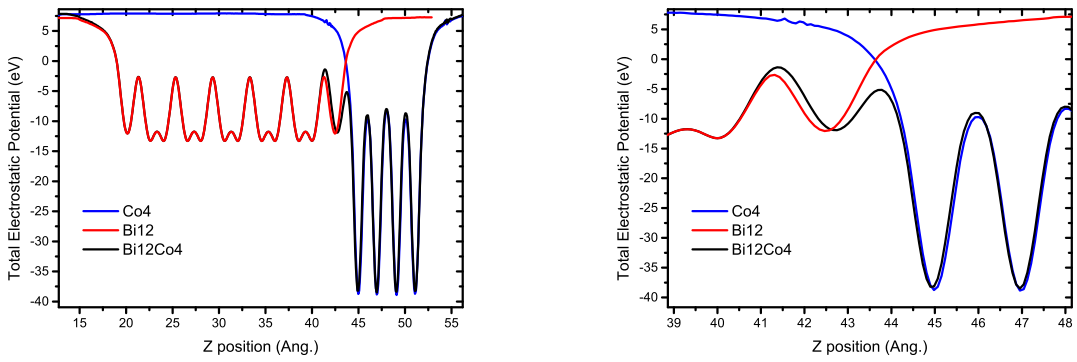

Figure A.5 – (a) Electrostatic potential along the Bi12Co4 supercell(Black), Cobalt Slab (blue) and Bismuth slab (red).In (b) a zoom close to the interface.

A.6 Magnetic Moments

In Figure A.6 is presented the magnetic moments along the simulated supercell (Bi12Co4). In red, the magnetic moment from the Bismuth only slab, showing no magnetic moment, as expected. In Blue, the magnetic moment from the Co slab, showing an increase of the magnetic moment at the surface. Im black the magnetic moments from supercell, which indicate that in the Bi/Co interface, there is an increase of the magnetic moment of bismuth atoms, down to the 4th layer of bismuth below the Co interface. Such long magnetic proximity effect is not only related to the hybridization at the interface but also to the bismuth electron occupation, which is changed in the vicinity of the interface, as described in the section above about the electrostatic potential. The magnetic moment of Cobalt atoms near to the interface also changes. The Cobalt close bond to the Bi atoms at the interface shows a decrease of magnetic moment, while the Co atom which a far from the Bi show almost the same moment as the one at the surface.

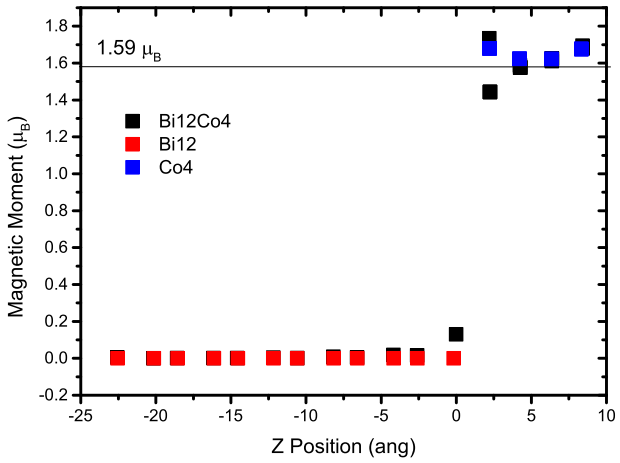

Figure A.6 – Magnetic moment per site at the Bi12Co4 supercell(Black), Cobalt Slab (blue) and Bismuth slab (red).

A.7 Spin-Orbit Energy

The Figure A.7 is displayed the Spin-Orbit Energy (SOE) along the supercell. The SOC at cobalt sites are small compared to the Bismuth. The Red and black data are for the bismuth slab and Bi12Co4 supercell, respectively. At the Bi slab there is a strong increase of SOE close to the surfaces, which are related to orbital distortion and the inversion symmetry break. However, the same not occurs close to the interface. The Blue data it the SOE for the Cobalt slab. The Figure 5.3, at the discussion section show the difference between the SOE from Supercell and the

Co slab. One can see that the SOE is high for the cobalt atoms close to the interface in relation to the Co atoms at the surface. Such SOE difference firstly decay to zero far from the interface. Such proximity effect is related to tho Co/Bi hybridization at the interface.

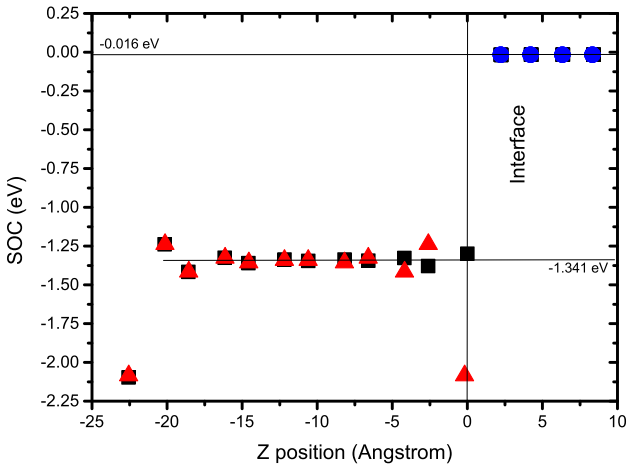

Figure A.7 – Spin-Orbit Energy for the Bi12Co4 supercell(Black), Cobalt Slab (blue) and Bismuth slab (red).

Bibliography

1 MANCHON, A. et al. New perspectives for rashba spin-orbit coupling. **Nature materials**, v. 14, 07 2015.

2 ZHANG, Y. et al. Manipulating effective spin orbit coupling based on proximity effect in magnetic bilayers. **Applied Physics Letters**, v. 107, 08 2015.

3 HONDA, S.; NAGATA, Y. Magnetic and transport properties of alternately deposited co-bi films. **Journal of Applied Physics**, v. 93, p. 5538–5542, 05 2003.

4 COEY, J.; COEY, J. **Magnetism and Magnetic Materials**. Cambridge University Press, 2010. (Knovel Library). ISBN 9780521816144. Disponível em: <https://books.google.com.br/books?id=Ie72CFd-eSEC>.

5 DEMTRÖDER, W. **Atoms, Molecules and Photons: An Introduction to Atomic-, Molecular- and Quantum Physics**. Springer Berlin Heidelberg, 2010. (Graduate Texts in Physics). ISBN 9783642102981. Disponível em: <https://books.google.com.br/books?id=vbc5mA7OEuYC>.

6 TAKAYAMA, A. Anomalous rashba effect of bi thin film studied by spin-resolved arpes. In: . [S.l.: s.n.], 2017.

7 LOPES, R. F. **Configurações complexas de spins em flmes finos heteroestruturas**. Tese (Doutorado) — Universidade Federal do Rio Grande do Sul, 2017.

8 NAGAOSA, N. et al. Anomalous hall effect. **Rev. Mod. Phys.**, American Physical Society, v. 82, p. 1539–1592, May 2010. Disponível em: <https://link.aps.org/doi/10.1103/RevModPhys.82.1539>.

9 KELLY, P.; ARNELL, R. Magnetron sputtering: a review of recent developments and applications. **Vacuum**, v. 56, n. 3, p. 159–172, 2000. ISSN 0042-207X. Disponível em: <https://www.sciencedirect.com/science/article/pii/S0042207X9900189X>.

10 RIGAKU.COM. <https://www.rigaku.com/de/node/713>. Accessed: 2021-10-15.

11 CHU, W.-K.; MAYER, J. W.; NICOLET, M.-A. Chapter 4 - backscattering spectrometry of thin films. In: CHU, W.-K.; MAYER, J. W.; NICOLET, M.-A. (Ed.). **Backscattering Spectrometry**. Academic Press, 1978. p. 89–122. ISBN 978-0-12-173850-1. Disponível em: <https://www.sciencedirect.com/science/article/pii/B9780121738501500090>.

12 Lopez-Dominguez, V. et al. A simple vibrating sample magnetometer for macroscopic samples. **Review of Scientific Instruments**, v. 89, n. 3, p. 034707, mar. 2018.

13 FERT, A.; CROS, V.; SAMPAIO, J. Skyrmions on the track. **Nature nanotechnology**, v. 8, p. 152–6, 03 2013.

14 LIU, C.-X.; ZHANG, S.-C.; QI, X.-L. The quantum anomalous hall effect: Theory and experiment. **Annual Review of Condensed Matter Physics**, v. 7, n. 1, p. 301–321, 2016. Disponível em: <https://doi.org/10.1146/annurev-conmatphys-031115-011417>.

15 HE, K.; WANG, Y.; XUE, Q.-K. Quantum anomalous Hall effect. **National Science Review**, v. 1, n. 1, p. 38–48, 12 2013. ISSN 2095-5138. Disponível em: <https://doi.org/10.1093/nsr/nwt029>.

16 HELLMAN, F. et al. Interface-induced phenomena in magnetism. **Rev. Mod. Phys.**, American Physical Society, v. 89, p. 025006, Jun 2017. Disponível em: <https://link.aps.org/doi/10.1103/RevModPhys.89.025006>.

17 METAXAS, P. J. et al. Creep and flow regimes of magnetic domain-wall motion in ultrathin $\mathrm{Pt/Co/Pt}$ films with perpendicular anisotropy. **Phys. Rev. Lett.**, American Physical Society, v. 99, p. 217208, Nov 2007. Disponível em: <https://link.aps.org/doi/10.1103/PhysRevLett.99.217208>.

18 FERT, A.; REYREN, N.; CROS, V. Magnetic skyrmions: advances in physics and potential applications. **Nature Reviews Materials**, Nature Publishing Group, v. 2, n. 7, p. 17031, jun. 2017. Disponível em: <https://hal.archives-ouvertes.fr/hal-02076548>.

19 DZYALOSHINSKY, I. A thermodynamic theory of "weak" ferromagnetism of antiferromagnetics. **Journal of Physics and Chemistry of Solids**, v. 4, n. 4, p. 241–255, 1958. ISSN 0022-3697. Disponível em: <https://www.sciencedirect.com/science/article/pii/0022369758900763>.

20 MORIYA, T. Anisotropic superexchange interaction and weak ferromagnetism. **Phys. Rev.**, American Physical Society, v. 120, p. 91–98, Oct 1960. Disponível em: <https://link.aps.org/doi/10.1103/PhysRev.120.91>.

21 MOKHTARI, I. B.-E. et al. Perpendicular magnetic anisotropy and interfacial dzyaloshinskii–moriya interaction in as grown and annealed x/co/y ultrathin systems. IOP Publishing, v. 32, n. 49, p. 495802, sep 2020. Disponível em: <https://doi.org/10.1088/1361-648x/abb0a8>.

22 SAMARDAK, A. S. et al. Enhancement of perpendicular magnetic anisotropy and Dzyaloshinskii–Moriya interaction in thin ferromagnetic films by atomic-scale modulation of interfaces. **NPG Asia Materials**, v. 12, n. 1, p. 51, jul. 2020.

23 IKEDA, S. et al. A perpendicular-anisotropy CoFeB–MgO magnetic tunnel junction. **Nature Materials**, v. 9, n. 9, p. 721–724, set. 2010.

24 WANG, L. et al. Construction of a room-temperature pt/co/ta multilayer film with ultrahigh-density skyrmions for memory application. **ACS Applied Materials & Interfaces**, v. 11, n. 12, p. 12098–12104, 2019. Disponível em: <https://doi.org/10.1021/acsami.9b00155>.

25 SCHULZ, T. et al. Emergent electrodynamics of skyrmions in a chiral magnet. **Nature Physics**, v. 8, n. 4, p. 301–304, abr. 2012.

26 NAGAOSA, N.; TOKURA, Y. Topological properties and dynamics of magnetic skyrmions. **Nature Nanotechnology**, v. 8, n. 12, p. 899–911, dez. 2013.

27 EMORI, S. et al. Current-driven dynamics of chiral ferromagnetic domain walls. **Nature Materials**, v. 12, n. 7, p. 611–616, jul. 2013.

28 SHAHBAZI, K. et al. Domain-wall motion and interfacial dzyaloshinskii-moriya interactions in $\mathrm{Pt/Co/Ir}(t_{\mathrm{ir}})\mathrm{/Ta}$ multilayers. **Phys. Rev. B**, American Physical Society, v. 99, p. 094409, Mar 2019. Disponível em: <https://link.aps.org/doi/10.1103/PhysRevB.99.094409>.

29 ŠčEPKA, T. et al. **Damping in Ru/Co-based multilayer films with large Dzyaloshinskii-Moriya interaction**. 2019.

30 VOLKOV, O. M. et al. Domain-wall damping in ultrathin nanostripes with dzyaloshinskii-moriya interaction. **Phys. Rev. Applied**, American Physical Society, v. 15, p. 034038, Mar 2021. Disponível em: <https://link.aps.org/doi/10.1103/PhysRevApplied.15.034038>.

31 SHAHBAZI, K. et al. Domain-wall motion and interfacial dzyaloshinskii-moriya interactions in $\mathrm{Pt/Co/Ir}(t_{\mathrm{ir}})\mathrm{/Ta}$ multilayers. **Phys. Rev. B**, American Physical Society, v. 99, p. 094409, Mar 2019. Disponível em: <https://link.aps.org/doi/10.1103/PhysRevB.99.094409>.

32 LOPES, R. et al. Spin textures and magnetotransport properties in cobalt/ruthenium and cobalt/palladium bilayers. **Journal of Magnetism and Magnetic Materials**, v. 519, p. 167447, 2021. ISSN 0304-8853. Disponível em: <https://www.sciencedirect.com/science/article/pii/S0304885320324148>.

33 ZHANG, W. et al. Tunable interfacial dzyaloshinskii–moriya interaction in symmetrical au/[fe/au]n multilayers. **Nanoscale**, The Royal Society of Chemistry, v. 13, p. 2665–2672, 2021. Disponível em: <http://dx.doi.org/10.1039/D0NR06488B>.

34 MANGIN, S. et al. Current-induced magnetization reversal in nanopillars with perpendicular anisotropy. **Nature Materials**, v. 5, n. 3, p. 210–215, Mar 2006. ISSN 1476-4660. Disponível em: <https://doi.org/10.1038/nmat1595>.

35 HONG, J. et al. On the perpendicular anisotropy of co/pd multilayers. **Journal of Magnetism and Magnetic Materials**, v. 285, n. 3, p. 359–366, 2005. ISSN 0304-8853. Disponível em: <https://www.sciencedirect.com/science/article/pii/S0304885304008327>.

36 KLOSE, C. et al. Optimization of spin-triplet supercurrent in ferromagnetic josephson junctions. **Phys. Rev. Lett.**, American Physical Society, v. 108, p. 127002, Mar 2012. Disponível em: <https://link.aps.org/doi/10.1103/PhysRevLett.108.127002>.

37 KHAIRE, T. et al. Observation of spin-triplet superconductivity in co-based josephson junctions. **Physical review letters**, v. 104, p. 137002, 04 2010.

38 AMUNDSEN, M.; LINDER, J. Quasiclassical theory for interfaces with spin-orbit coupling. **Phys. Rev. B**, American Physical Society, v. 100, p. 064502, Aug 2019. Disponível em: <https://link.aps.org/doi/10.1103/PhysRevB.100.064502>.

39 KATMIS, F. et al. A high-temperature ferromagnetic topological insulating phase by proximity coupling. **Nature**, v. 533, n. 7604, p. 513–516, May 2016. ISSN 1476-4687. Disponível em: <https://doi.org/10.1038/nature17635>.

40 AVSAR, A. et al. Spin–orbit proximity effect in graphene. **Nature Communications**, v. 5, n. 1, p. 4875, Sep 2014. ISSN 2041-1723. Disponível em: <https://doi.org/10.1038/ncomms5875>.

41 LIN, W. et al. Interface-based tuning of rashba spin-orbit interaction in asymmetric oxide heterostructures with 3d electrons. **Nature Communications**, v. 10, n. 1, p. 3052, Jul 2019. ISSN 2041-1723. Disponível em: <https://doi.org/10.1038/s41467-019-10961-z>.

42 LÓPEZ, A. et al. Proximity-induced spin-orbit effects in graphene on au. **Phys. Rev. B**, American Physical Society, v. 99, p. 085411, Feb 2019. Disponível em: <https://link.aps.org/doi/10.1103/PhysRevB.99.085411>.

43 KLIMOVSKIKH, I. I. et al. Spin–orbit coupling induced gap in graphene on pt(111) with intercalated pb monolayer. **ACS Nano**, American Chemical Society, v. 11, n. 1, p. 368–374, Jan 2017. ISSN 1936-0851. Disponível em: <https://doi.org/10.1021/acsnano.6b05982>.

44 SŁAWIŃSKA, J.; CERDÁ, J. I. Spin–orbit proximity effect in graphene on metallic substrates: decoration versus intercalation with metal adatoms. IOP Publishing, v. 21, n. 7, p. 073018, jul 2019. Disponível em: <https://doi.org/10.1088/1367-2630/ab2bc7>.

45 ISLAND, J. O. et al. Spin–orbit-driven band inversion in bilayer graphene by the van der waals proximity effect. **Nature**, v. 571, n. 7763, p. 85–89, Jul 2019. ISSN 1476-4687. Disponível em: <https://doi.org/10.1038/s41586-019-1304-2>.

46 EWING, J. Ii. on time-lag in the magnetisation of iron. **Proceedings of the Royal Society of London**, v. 46, p. 269 – 286.

47 KITTEL, C. **Introduction to Solid State Physics**. 8. ed. Wiley, 2004. ISBN 9780471415268. Disponível em: <http://www.amazon.com/Introduction-Solid-Physics-Charles-Kittel/dp/047141526X/ref=dp_ob_title_bk>.

48 HELLMAN, F. et al. Interface-induced phenomena in magnetism. **Rev. Mod. Phys.**, American Physical Society, v. 89, p. 025006, Jun 2017. Disponível em: <https://link.aps.org/doi/10.1103/RevModPhys.89.025006>.

49 GRIFFITHS, D. J. **Introduction to Quantum Mechanics (2nd Edition)**. 2nd. ed. Pearson Prentice Hall, 2004. Hardcover. ISBN 0131118927. Disponível em: <http://www.amazon.com/exec/obidos/redirect?tag=citeulike07-20&path=ASIN/0131118927>.

50 VEEDU, S.; POPOVIC, Z.; SATPATHY, s. Theoretical model for rashba spin-orbit interaction in d electrons. **Physical Review B**, v. 90, 10 2014.

51 MANCHON, A. et al. New perspectives for rashba spin–orbit coupling. **Nature Materials**, v. 14, n. 9, p. 871–882, Sep 2015. ISSN 1476-4660. Disponível em: <https://doi.org/10.1038/nmat4360>.

52 BIHLMAYER, G.; RADER, O.; WINKLER, R. Focus on the rashba effect. IOP Publishing, v. 17, n. 5, p. 050202, may 2015. Disponível em: <https://doi.org/10.1088/1367-2630/17/5/050202>.

53 DRESSELHAUS, G. Spin-orbit coupling effects in zinc blende structures. **Phys. Rev.**, American Physical Society, v. 100, p. 580–586, Oct 1955. Disponível em: <https://link.aps.org/doi/10.1103/PhysRev.100.580>.

54 BYCHKOV, Y.; RASHBA, E. Properties of a 2d electron gas with lifted spectral degeneracy. In: . [S.l.: s.n.], 1984.

55 SCHäPERS, T. **Semiconductor Spintronics**. De Gruyter, 2021. ISBN 9783110639001. Disponível em: <https://doi.org/10.1515/9783110639001>.

56 MEIER, F. **Rashba-type spin-orbit coupling in the surface alloys on ag(111) probed by spin- and angle-resolved photoemission spectroscopy**. Dissertação (Mestrado) — University of Zurich, Faculty of Science., 2011.

57 ASHCROFT, N.; MERMIN, N. **Solid State Physics**. Fort Worth: Saunders College Publishing, 1976.

58 PIPPARD, A. B. Magnetoresistance in metals. In: . [S.l.: s.n.], 1989.

59 CAMPBELL, I. A.; FERT, A.; JAOUL, O. The spontaneous resistivity anisotropy in ni-based alloys. **Journal of Physics C: Solid State Physics**, IOP Publishing, v. 3, n. 1S, p. S95–S101, may 1970. Disponível em: <https://doi.org/10.1088/0022-3719/3/1s/310>.

60 KOKADO, S. et al. Anisotropic magnetoresistance effects in fe, co, ni, fe4n, and half-metallic ferromagnet: A systematic analysis. **Journal of the Physical Society of Japan**, v. 81, n. 2, p. 024705, 2012. Disponível em: <https://doi.org/10.1143/JPSJ.81.024705>.

61 HALL, E. H. Xviii. on the "rotational coefficient" in nickel and cobalt. **Philosophical Magazine Series 1**, v. 12, p. 157–172.

62 Shiomi, Y. **Anomalous and Topological Hall Effects in Itinerant Magnets**. [S.l.: s.n.], 2013.

63 NAGAOSA, N. et al. Anomalous hall effect. **Rev. Mod. Phys.**, American Physical Society, v. 82, p. 1539–1592, May 2010. Disponível em: <https://link.aps.org/doi/10.1103/RevModPhys.82.1539>.

64 KARPLUS, R.; LUTTINGER, J. M. Hall effect in ferromagnetics. **Phys. Rev.**, American Physical Society, v. 95, p. 1154–1160, Sep 1954. Disponível em: <https://link.aps.org/doi/10.1103/PhysRev.95.1154>.

65 SMIT, J. The spontaneous hall effect in ferromagnetics i. **Physica**, v. 21, n. 6, p. 877–887, 1955. ISSN 0031-8914. Disponível em: <https://www.sciencedirect.com/science/article/pii/S0031891455925969>.

66 SMIT, J. The spontaneous hall effect in ferromagnetics ii. **Physica**, v. 24, n. 1, p. 39–51, 1958. ISSN 0031-8914. Disponível em: <https://www.sciencedirect.com/science/article/pii/S0031891458935419>.

67 BERGER, L. Influence of spin-orbit interaction on the transport processes in ferromagnetic nickel alloys, in the presence of a degeneracy of the 3d band. **Physica**, v. 30, n. 6, p. 1141–1159, 1964. ISSN 0031-8914. Disponível em: <https://www.sciencedirect.com/science/article/pii/0031891464901053>.

68 BRUNDLE, C. et al. **Encyclopedia of Materials Characterization: Surfaces, Interfaces, Thin Films**. Butterworth-Heinemann, 1992. (Characterization Series). ISBN 9780750691680. Disponível em: <https://books.google.com.br/books?id=i7XYEp0TVc4C>.

69 VERMA, H. **Atomic and Nuclear Analytical Methods: XRF, Mössbauer, XPS, NAA and Ion-Beam Spectroscopic Techniques**. Springer Berlin Heidelberg, 2007. ISBN 9783540302797. Disponível em: <https://books.google.com.br/books?id=JmK6IaBCyOIC>.

70 ECKSTEIN, W.; MAYER, M. Rutherford backscattering from layered structures beyond the single scattering model. **Nuclear Instruments and Methods in Physics Research Section B, Beam Interactions with Materials and Atoms**, Netherlands, v. 153, n. 1-4, p. 337–344, 1999. ISSN 0168-583X. ATOMIC AND MOLECULAR PHYSICS. Disponível em: <http://inis.iaea.org/search/search.aspx?orig_q=RN:33038832>.

71 Foner, S. Versatile and Sensitive Vibrating-Sample Magnetometer. **Review of Scientific Instruments**, v. 30, n. 7, p. 548–557, jul. 1959.

72 LOPEZ-DOMINGUEZ, V. et al. A simple vibrating sample magnetometer for macroscopic samples. **Review of Scientific Instruments**, v. 89, n. 3, p. 034707, 2018. Disponível em: <https://doi.org/10.1063/1.5017708>.

73 TENCÉ, S. et al. CoBi3–the first binary compound of cobalt with bismuth: high-pressure synthesis and superconductivity. IOP Publishing, v. 26, n. 39, p. 395701, sep 2014. Disponível em: <https://doi.org/10.1088/0953-8984/26/39/395701>.

74 MASOOD, A. et al. Co-based amorphous thin films on silicon with soft magnetic properties. **AIP Advances**, v. 8, n. 5, p. 056109, 2018. Disponível em: <https://doi.org/10.1063/1.5007733>.

75 JIAO, D. et al. Microstructures and magnetic properties of cobalt thin films. **Modern Physics Letters B - MOD PHYS LETT B**, v. 22, p. 3079–3086, 12 2008.

76 VAHAPLAR, K. et al. Effect of ta buffer layer and thickness on the structural and magnetic properties of co thin films. **Journal of Vacuum Science Technology B: Microelectronics and Nanometer Structures**, v. 27, p. 2112–2116, 09 2009.

77 CHOWDHURY, N.; BEDANTA, S. Controlling the anisotropy and domain structure with oblique deposition and substrate rotation. In: . [S.l.: s.n.], 2015. p. 1–1.

78 COJOCARU, S.; NADDEO, A.; CITRO, R. Modification of the bloch law in ferromagnetic nanostructures. IOP Publishing, v. 106, n. 1, p. 17001, mar 2014. Disponível em: <https://doi.org/10.1209/0295-5075/106/17001>.

79 SCHNEIDER, C. M. et al. Curie temperature of ultrathin films of fcc-cobalt epitaxially grown on atomically flat cu(100) surfaces. **Phys. Rev. Lett.**, American Physical Society, v. 64, p. 1059–1062, Feb 1990. Disponível em: <https://link.aps.org/doi/10.1103/PhysRevLett.64.1059>.

80 ZHANG, R.; WILLIS, R. F. Thickness-dependent curie temperatures of ultrathin magnetic films: Effect of the range of spin-spin interactions. **Phys. Rev. Lett.**, American Physical Society, v. 86, p. 2665–2668, Mar 2001. Disponível em: <https://link.aps.org/doi/10.1103/PhysRevLett.86.2665>.

81 JIANG, Q.; YANG, H.-N.; WANG, G.-C. Effect of interface roughness on hysteresis loops of ultrathin co films from 2 to 30 ml on cu(001) surfaces. **Surface Science**, v. 373, n. 2, p. 181–194, 1997. ISSN 0039-6028. Disponível em: <https://www.sciencedirect.com/science/article/pii/S0039602896011624>.

82 BRANDãO, J. et al. Understanding the role of damping and dzyaloshinskii-moriya interaction on dynamic domain wall behaviour in platinum-ferromagnet nanowires. **Scientific Reports**, v. 7, 12 2017.

83 FERNÁNDEZ-PACHECO, A. et al. Symmetry-breaking interlayer dzyaloshinskii–moriya interactions in synthetic antiferromagnets. **Nature Materials**, v. 18, n. 7, p. 679–684, Jul 2019. ISSN 1476-4660. Disponível em: <https://doi.org/10.1038/s41563-019-0386-4>.

84 OSMAN, N. S. E.; MOYO, T. Temperature dependence of coercivity and magnetization of sr1/3mn1/3co1/3fe2o4 ferrite nanoparticles. **Journal of Superconductivity and Novel Magnetism**, v. 29, n. 2, p. 361–366, Feb 2016. ISSN 1557-1947. Disponível em: <https://doi.org/10.1007/s10948-015-3227-y>.

85 MENDONçA, E. C. et al. Temperature dependence of coercive field of znfe2o4 nanoparticles. **Journal of Applied Physics**, v. 111, n. 5, p. 053917, 2012. Disponível em: <https://doi.org/10.1063/1.3691792>.

86 De Vries, J. Temperature and thickness dependence of the resistivity of thin polycrystalline aluminium, cobalt, nickel, palladium, silver and gold films. **Thin Solid Films**, v. 167, n. 1, p. 25–32, 1988. ISSN 0040-6090. Disponível em: <https://www.sciencedirect.com/science/article/pii/0040609088904786>.

87 GLEBOVSKY, V. et al. Electron-beam floating zone growing of high-purity cobalt crystals. **Materials Letters**, v. 36, n. 5, p. 308–314, 1998. ISSN 0167-577X. Disponível em: <https://www.sciencedirect.com/science/article/pii/S0167577X98000500>.

88 GALLO, C. F.; CHANDRASEKHAR, B. S.; SUTTER, P. H. Transport properties of bismuth single crystals. **Journal of Applied Physics**, v. 34, n. 1, p. 144–152, 1963. Disponível em: <https://doi.org/10.1063/1.1729056>.

89 YANG, F. Y. et al. Large magnetoresistance of electrodeposited single-crystal bismuth thin films. **Science**, v. 284, n. 5418, p. 1335–1337, 1999.

90 XIAO, S.; WEI, D.; JIN, X. Bi(111) thin film with insulating interior but metallic surfaces. **Phys. Rev. Lett.**, American Physical Society, v. 109, p. 166805, Oct 2012. Disponível em: <https://link.aps.org/doi/10.1103/PhysRevLett.109.166805>.

91 BHATIA, E. et al. Superconductivity, kondo effect, and observation of self-organized pattern formation in intermetallic nibi3 thin films. **Intermetallics**, v. 94, p. 160–164, 2018. ISSN 0966-9795. Disponível em: <https://www.sciencedirect.com/science/article/pii/S0966979517308725>.

92 IRFAN, B.; CHATTERJEE, R. Magneto-transport and kondo effect in cobalt doped bi2se3 topological insulators. **Applied Physics Letters**, v. 107, n. 17, p. 173108, 2015. Disponível em: <https://doi.org/10.1063/1.4934569>.

93 CRACO, L.; LEONI, S. Magnetoresistance in the spin-orbit kondo state of elemental bismuth. **Scientific Reports**, v. 5, n. 1, p. 13772, Sep 2015. ISSN 2045-2322. Disponível em: <https://doi.org/10.1038/srep13772>.

94 HOU, D. et al. The anomalous hall effect in epitaxial face-centered-cubic cobalt films. **Journal of Physics: Condensed Matter**, IOP Publishing, v. 24, n. 48, p. 482001, oct 2012. Disponível em: <https://doi.org/10.1088/0953-8984/24/48/482001>.

95 KÖTZLER, J.; GIL, W. Anomalous hall resistivity of cobalt films: Evidence for the intrinsic spin-orbit effect. **Phys. Rev. B**, American Physical Society, v. 72, p. 060412, Aug 2005. Disponível em: <https://link.aps.org/doi/10.1103/PhysRevB.72.060412>.

96 KOBS, A. et al. Anisotropic interface magnetoresistance in $\mathrm{Pt/Co/Pt}$ sandwiches. **Phys. Rev. Lett.**, American Physical Society, v. 106, p. 217207, May 2011. Disponível em: <https://link.aps.org/doi/10.1103/PhysRevLett.106.217207>.

97 TOKAç, M. et al. Interfacial contribution to thickness dependent in-plane anisotropic magnetoresistance. **AIP Advances**, v. 5, n. 12, p. 127108, 2015. Disponível em: <https://doi.org/10.1063/1.4937556>.

98 LIU, Y. F.; CAI, J. W.; SUN, L. Large enhancement of anisotropic magnetoresistance and thermal stability in ta/nife/ta trilayers with interfacial pt addition. **Applied Physics Letters**, v. 96, n. 9, p. 092509, 2010. Disponível em: <https://doi.org/10.1063/1.3334720>.

99 ZHANG, P. et al. Anomalous hall effect in co/ni multilayers with perpendicular magnetic anisotropy. **Applied Physics Letters**, v. 104, n. 8, p. 082404, 2014. Disponível em: <https://doi.org/10.1063/1.4866774>.

100 BASEDEN, K. A.; TYE, J. W. Introduction to density functional theory: Calculations by hand on the helium atom. **Journal of Chemical Education**, v. 91, n. 12, p. 2116–2123, 2014. Disponível em: <https://doi.org/10.1021/ed5004788>.

101 HAFNER, J.; KRESSE, G. The vienna ab-initio simulation program vasp: An efficient and versatile tool for studying the structural, dynamic, and electronic properties of materials. In: ____. **Properties of Complex Inorganic Solids**. Boston, MA: Springer US, 1997. p. 69–82. ISBN 978-1-4615-5943-6. Disponível em: <https://doi.org/10.1007/978-1-4615-5943-6_10>.

102 KOHN, W.; SHAM, L. J. Self-consistent equations including exchange and correlation effects. **Phys. Rev.**, American Physical Society, v. 140, p. A1133–A1138, Nov 1965. Disponível em: <https://link.aps.org/doi/10.1103/PhysRev.140.A1133>.

103 BLÖCHL, P. E. Projector augmented-wave method. **Phys. Rev. B**, American Physical Society, v. 50, p. 17953–17979, Dec 1994. Disponível em: <https://link.aps.org/doi/10.1103/PhysRevB.50.17953>.

104 PERDEW, J. P.; BURKE, K.; ERNZERHOF, M. Generalized gradient approximation made simple. **Phys. Rev. Lett.**, American Physical Society, v. 77, p. 3865–3868, Oct 1996. Disponível em: <https://link.aps.org/doi/10.1103/PhysRevLett.77.3865>.

105 PERDEW, J. P.; WANG, Y. Accurate and simple analytic representation of the electron-gas correlation energy. **Phys. Rev. B**, American Physical Society, v. 45, p. 13244–13249, Jun 1992. Disponível em: <https://link.aps.org/doi/10.1103/PhysRevB.45.13244>.

106 ZHAO, G. L.; BAGAYOKO, D.; WILLIAMS, T. D. Local-density-approximation prediction of electronic properties of gan, si, c, and $\mathrm{ruo_2}$. **Phys. Rev. B**, American Physical Society, v. 60, p. 1563–1572, Jul 1999. Disponível em: <https://link.aps.org/doi/10.1103/PhysRevB.60.1563>.

107 ZHANG, G.-X. et al. Performance of various density-functional approximations for cohesive properties of 64 bulk solids. **New Journal of Physics**, IOP Publishing, v. 20, n. 6, p. 063020, jun 2018. Disponível em: <https://doi.org/10.1088/1367-2630/aac7f0>.